AN ABSTRACT OF THE THESIS OF

Eric M. Becker for the degree of Master of Science in Radiation Health Physics presented on August 19, 2013.

Title: The MiniSpec: A Low-Cost, Compact, FPGA-Based Gamma Spectrometer for Mobile Applications

Abstract approved:

Abdollah T. Farsoni

There is a significant role in emergency response and personal radiation safety that can be played by a compact radiation detector that is capable of identifying radionuclides. Herein is described the design, construction, and characterization of a small, low-cost, low-power gamma ray spectrometer prototype intended to fill this role, conducted in the Advanced Radiation Instrumentation Laboratory at Oregon State University. This spectrometer uses a CsI(Tl) scintillation crystal coupled to a solid-state photomultiplier to detect radiation interactions and an on-board 40 MHz, 12-bit digital pulse-processor based on a field-programmable gate array that generates an energy histogram. The spectrometer is designed be accessed wirelessly to allow a mobile phone to connect to it to display the data. The device requires a single 3.7 V input and consumes only 300 mA when programmed, allowing it to be powered by a mobile phone battery. The full

device is estimated to be 5 x 10 x 5 cm and weighs approximately 12 oz. This device is able to achieve 5.66% FWHM energy resolution at 662 keV.

The MiniSpec: A Low-Cost, Compact, FPGA-Based Gamma Spectrometer for Mobile Applications

by

Eric M. Becker

A THESIS

submitted to

Oregon State University

in partial fulfillment of

the requirements for the

degree of

Master of Science

Presented August 19, 2013

Commencement June 2014

Master of Science thesis of Eric M. Becker presented on August 19, 2013.

APPROVED:

Major Professor, representing Radiation Health Physics

Head of the Department of Nuclear Engineering and Radiation Health Physics

---

Dean of the Graduate School

I understand that my thesis will become part of the permanent collection of Oregon State University libraries. My signature below authorizes release of my thesis to any reader upon request.

Eric M. Becker, Author

ACKNOWLEDGEMENTS

to my family and friends, thank you for your support and encouragement. it helps to know that those important to you are behind you all the way.

to my parents, thank you for providing for my education all the way through my undergraduate career and always supporting my decisions. i cannot conceive of, much less ask for, better parents.

to my colleagues, thank you for your help completing this work. being able to bounce ideas off of others, especially late at night, was very helpful, both for this work and my peace of mind.

to Dr. Abi Farsoni, thank you for affording me the opportunity to work under your tutelage. i am grateful for the intellectual as well as financial support you have provided me for the past two years. you pushed me to learn a wealth of new skills and gain a deeper understanding of the systems i work with, which has matured my attitude toward the work i perform, an invaluable personal development.

TABLE OF CONTENTS

Page

LIST OF FIGURES

LIST OF FIGURES

LIST OF FIGURES

LIST OF FIGURES

LIST OF TABLES

THE MINISPEC: A LOW-COST, COMPACT, FPGA-BASED GAMMA SPECTROMETER FOR MOBILE APPLICATIONS

1. INTRODUCTION

1.1. Overview

Detection and identification of radionuclides as well as the quantity present in a given area are of great importance to many different nations, organizations, and individuals worldwide [1] [2] [3] [4] [5] [6] [7] [8]. Because gamma rays penetrate matter further than alpha or beta particles, gamma rays are an easier form of radiation emission to detect outside a controlled laboratory setting and at a distance from the source. In addition, gamma rays have characteristic energies that allow for identification of specific radioisotopes, unlike neutrons and beta particles, which have energy distributions. These properties are vital for performing gamma spectrometry, which is in turn vital to locating and identifying radionuclides [9] [10] [11] [12].

Gamma spectrometers commonly come in the form of relatively large devices that are confined to a laboratory and use Nuclear Instrumentation Modules (NIM) or other bulky signal processing electronics. While such devices might serve the needs of a nation or organization, they are often ill-suited for use as personal gamma spectroscopy devices because of their size, fixed arrangements, fragility, and cost. They also often require a personal computer or laptop equipped with a specialist program to display and analyze the spectra that result

from the measurements, making such devices more unwieldy for fast, everyday use.

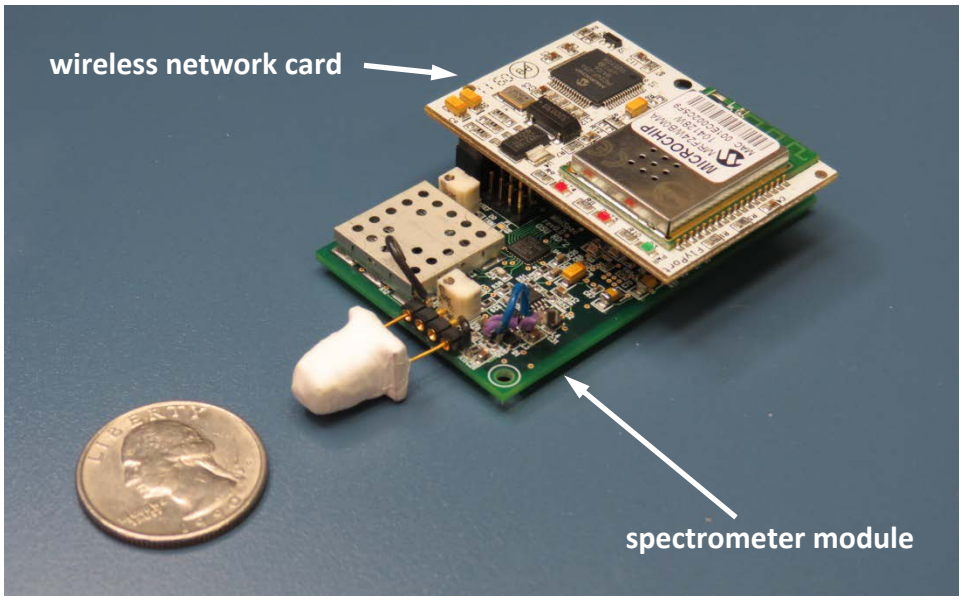

Figure 1. The MiniSpec prototype device, with U.S. quarter for scale.

The device described herein is designed to be small, low-cost, and require only that the user have access to a wireless-capable device. The prototype device is shown in figure 1. The key components that facilitate these features are a solid-state photomultiplier (SSPM) for scintillation light collection and a field-programmable gate array (FPGA) that conducts all signal processing, data storage, and external interfacing. These two devices, with a CsI(Tl) scintillation crystal coupled to the SSPM, are integrated onto a printed circuit board (PCB), which also contains the power regulators, analog amplification components, analog-to-digital converter, programmable read-only memory (PROM), temperature sensor, and input/output (I/O) headers. This PCB will henceforth be referred to as the “spectrometer module”. Other modules, such as the battery,

wireless network card, and USB interface, can be connected to the detector module via the I/O headers to form the complete functional design.

1.2. Goals

This work encompasses the design, construction, and characterization of a miniature gamma ray spectrometer prototype, the "MiniSpec". The spectrometer utilizes a CsI(Tl) scintillation crystal coupled to a SSPM as the detection component. An FPGA-based digital pulse processor performs the functions of MCA, data storage, and external communication. The power regulators, SSPM, analog amplification components, analog-to-digital converter, FPGA, supplemental components, and input/output headers are all located on a 3.81 cm x 6.35 cm PCB. A processing algorithm implemented in the FPGA was also developed for this device and constructed in VHDL. The device is able to use an external USB interface board for data acquisition, and can accommodate a wireless network card for display on a mobile device, though this is not implemented in this work. The specific areas of characterization for the complete device are

- optimum peaking and flat times of the digital trapezoidal shaper,
- dynamic gamma energy range,
- linearity in digital channel number with respect to energy,
- electronic noise,
- gamma-ray energy resolution,
- intrinsic photopeak efficiency, and
- efficacy of the digital pulse processing algorithm.

1.3. Applications

The MiniSpec can be used for a variety of applications that take advantage of its portability and wireless capability. Its primary intended use is for personal radiation monitoring in an emergency setting where identification of isotopes and their strength is important for determining the dose rate, and therefore risk, involved in being in a given area. Since the MiniSpec is designed to have wireless capability and be able to link directly to any wireless device, including mobile phones, data from different areas of an emergency can be quickly collated into an online map of the hazard distribution accessible to anyone. Other possible applications include battlefield monitoring for soldiers and isotope identification for border security.

2. LITERATURE REVIEW

2.1. Gamma Spectroscopy Using Scintillators

Gamma ray detection and measurement using scintillators is a technique that has been in use since the 1930s [13]. Therefore, the basic features of gamma ray spectra, the gamma ray interactions that cause them, and the principles of scintillator physics are well known, and explained below.

2.1.1. Full-Energy Peaks

Full-energy peaks can be the result of different manners of gamma ray interaction. One such manner is photoelectric absorption, in which a gamma ray interacts with an atom, completely disappearing and transferring all of its energy. An electron is then ejected from the atom with kinetic energy equal to the energy of the gamma ray that was absorbed minus the binding energy of the electron [14]. Because the gamma rays from a given isotope are characteristic, this will ideally result in a Dirac delta function at the energy of the absorbed gamma ray, E_γ, as depicted in figure 2. However, statistical fluctuations in the number of photons generated for a given amount of energy deposited in the scintillator mean that this peak will have a characteristic distribution in a real detector [15].

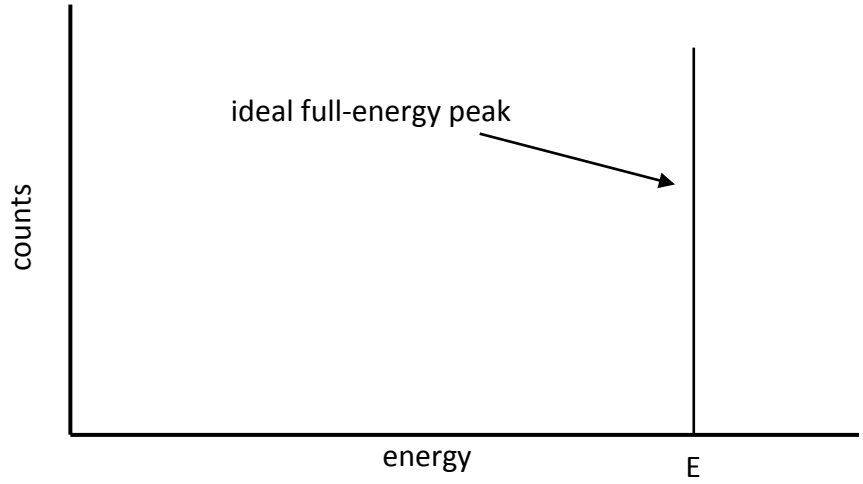

Figure 2. Ideal photoelectric absorption response resulting in an ideal full-energy peak. Based on Knoll, 2000 [15].

Sometimes, a combination of interactions other than photoelectric absorption may take place within the detection medium that nevertheless lead to deposition of all the original gamma ray's energy in the detector. In this case, the resulting "full-energy peak" will appear in the spectrum in the same place as the photopeak, one superimposed on the other. Indeed, a photopeak is essentially a sub-type of full-energy peak. Thus the term "full-energy peak" will be used to describe the peak resulting from all full-energy deposition events, including photoelectric absorption.

2.1.2. The Compton Continuum

First discovered by Arthur Compton, Compton scatter occurs when a gamma ray is incident on an electron in an atom and, like photoelectric absorption, transfers enough energy to overcome the electron's binding energy and eject the electron from the atom. However, only a part of the gamma ray's energy is lost, and the

gamma ray scatters at an angle that depends on the amount of energy imparted to the electron, as shown in (1).

$$E' = \frac{E}{1 + \frac{E}{m_0 c^2}(1 - \cos\vartheta)}, \tag{1}$$

where E is the initial energy of the incident gamma ray, E' is the energy of the scattered gamma ray, m_0c^2 is the rest-energy of an electron, and ϑ is the angle at which the gamma ray is scattered [16], as illustrated in figure 3.

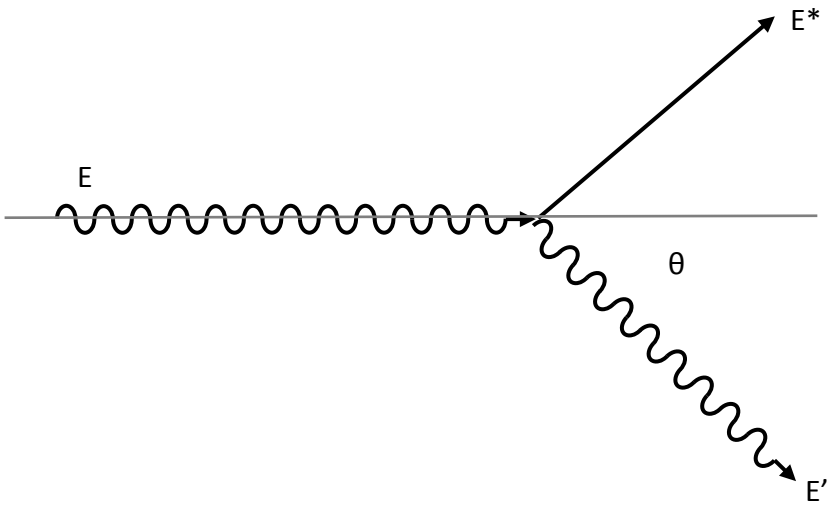

Figure 3. Compton scatter event diagram, based on Knoll, 2000 [15].

The energy transferred to the recoil electron during this process is $E^* = E - E'$, which is usually completely deposited in the detector bulk. The maximum amount of energy that can be deposited by the incident gamma ray occurs when the scattering angle is equal to 180°. However, even in this maximum case, not

all of the incident gamma ray's energy is absorbed and the scattered gamma can still escape the detector without depositing its full energy in the detector bulk [15]. The angle at which the gamma ray scatters is random, but possesses a distribution described by the Klein-Nishina cross-section [14]. In an ideal detector spectrum, this continuum extends from zero to the Compton edge, which is the energy absorbed in a Compton scatter when the angle of scatter is 180° [15]. The general shape of the Compton continuum for a single gamma energy is illustrated in figure 4. As with the full-energy peak, various effects will lead to a distribution in the Compton edge, giving it a rounded shape.

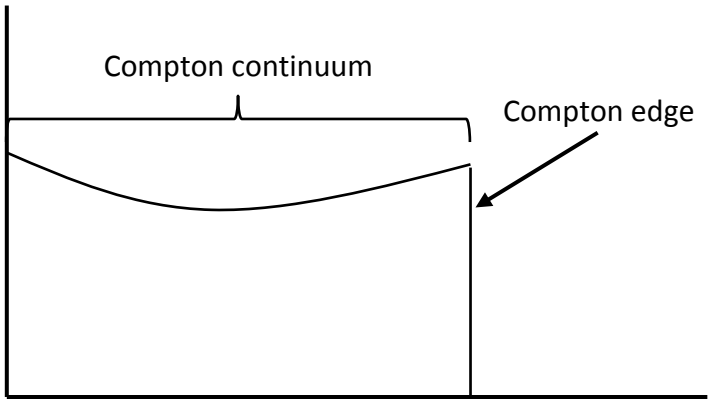

Figure 4. Diagram of ideal Compton continuum for a given gamma energy, based on Knoll, 2000 [15].

2.1.3. Escape Peaks

When a gamma ray with enough energy interacts with an atom, it may produce two electrons: one positron and one negatron. This mechanism is called pair production. The threshold energy for this gamma ray is 1022 keV since the rest energy of each electron is 511 keV. If the gamma ray energy is greater than 1022

keV, the excess energy will be split between the two electrons as kinetic energy. Typically, both particles are stopped in the detection medium. This results in deposited energy equal to the combined initial kinetic energy of the two particles, or, the incident gamma energy minus the rest mass energy of the two particles. However, since the positron is the anti-particle of the negatron, the positron will annihilate with a negatron when it loses its kinetic energy, resulting in the generation of two 511 keV gamma rays emitted in opposite directions [14] [15]. This interaction mechanism is illustrated in figure 5.

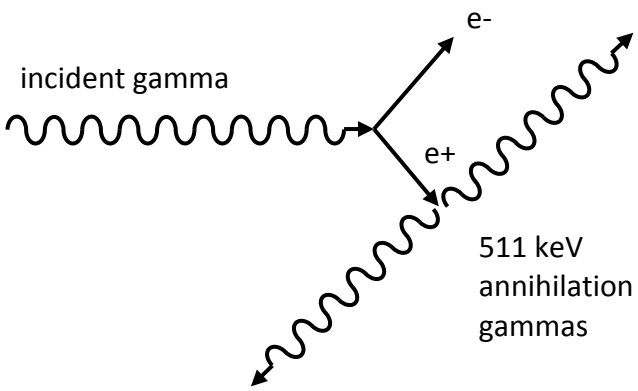

Figure 5. Diagram of pair production interaction, based on Knoll, 2000 [15].

Since real detectors are not of infinite size, there is a probability that one or both of the 511 keV gamma rays will escape the detection medium. If neither escapes, then the series of energy deposition events will appear on the gamma ray spectrum as a peak centered at the original incident gamma ray energy since these reactions occur so closely together in time. If one of the 511 keV gamma rays escapes, then a peak centered at the incident energy minus 511 keV will appear in the gamma spectrum. Similarly, if both 511 keV gamma rays escape the detector, then a peak centered at the incident energy minus 1022 keV will

appear in the gamma spectrum. These two peaks are commonly called single- and double-escape peaks, respectively [15]. These peaks often appear in the Compton continuum in a gamma spectrum, as illustrated in figure 6.

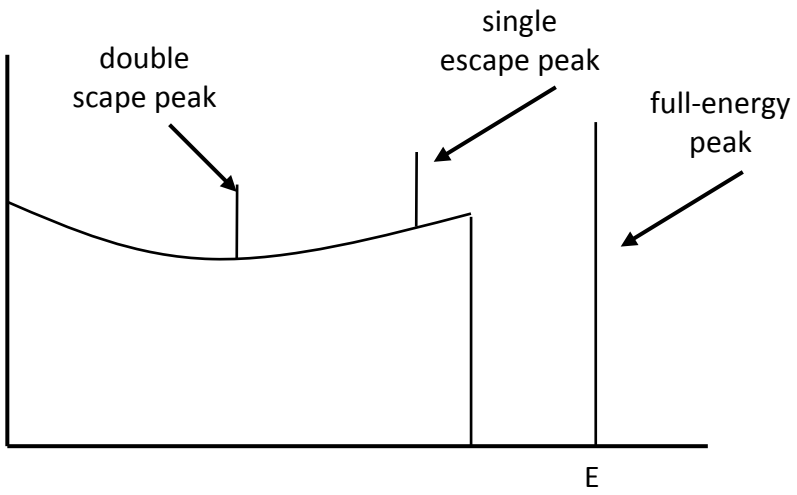

Figure 6. Illustration of single- and double-escape peaks resulting from pair production, based on Knoll, 2000 [15].

Pair production does not comprise a significant probability unless the material it interacts in has a high average atomic number. This is illustrated in figure 7. The relation between the atomic number of the interaction medium and the incident photon energy is also shown for photoelectric effect and Compton scatter events.

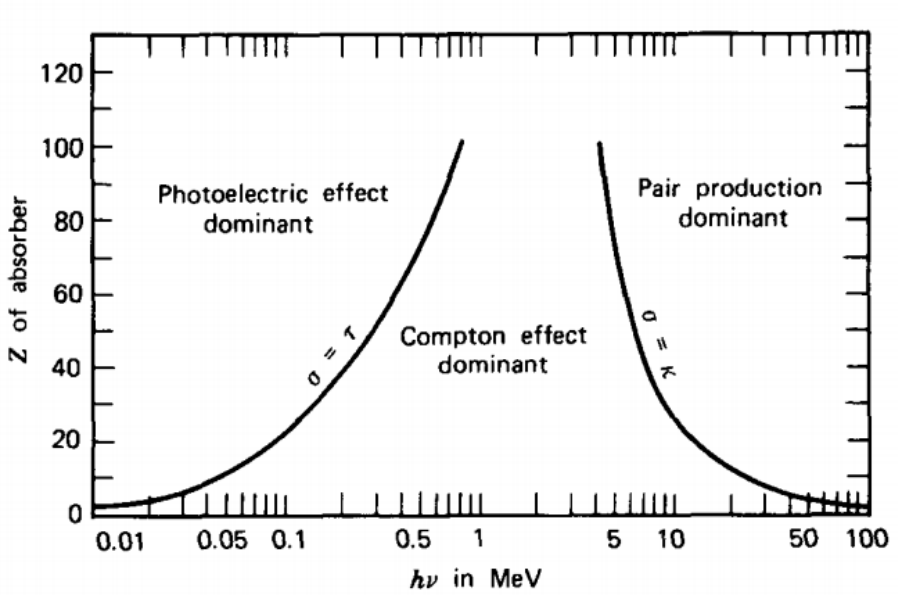

Figure 7. Regions of dominance for the three primary gamma interactions with matter, taken from Knoll, 2000 [15].

2.1.4. Scintillator Detector Principles

Scintillators refer to a class of materials that, upon stimulation by deposition of energy in the material, release photons. Scintillator materials fall into two general categories: organic and inorganic, named for the chemical composition of the materials. When radiation deposits energy in a scintillator, photons can be generated via three processes: prompt fluorescence, phosphorescence, and delayed fluorescence. Both types of fluorescence involve the emission of visible photons after excitement of the atoms of the material, though delayed fluorescence has a longer emission time. Phosphorescence also produces visible light, but at longer wavelengths and with longer emission times than fluorescence [15].

Inorganic scintillators are usually chosen for gamma spectroscopy because they are composed of elements with higher atomic numbers, which means they have greater efficiency for gamma rays [17]. In an inorganic scintillator, electrons in the valence energy band are excited across the bandgap to the conduction energy band by radiation energy deposition. When an electron in the conduction band de-excites and returns to the valence band, it releases its excitation energy as a photon. Since, in a pure crystal, these photons are usually outside the range of visible light [18], inorganic scintillators are usually doped with another element in order to produce visible light. The activator introduces energy levels between the bulk crystal's valence and conduction levels, allowing the photon to release a smaller amount of energy at one time, increasing the probability that a photon with a visible wavelength will be emitted [15]. This process is illustrated in figure 8.

The process above is the primary way in which light is emitted from the scintillator, or fluoresces. Phosphorescence occurs in inorganic scintillators when an excited electron becomes trapped in the material, unable to transfer to the valence band. Thermal excitation can provide enough energy for the electron to transfer out of this state, delaying the light emission, thereby causing phosphorescence instead of fluorescence [19]. Other mechanisms, such as quenching and exciton creation, can also occur instead of fluorescence, and may or may not cause light emission [15].

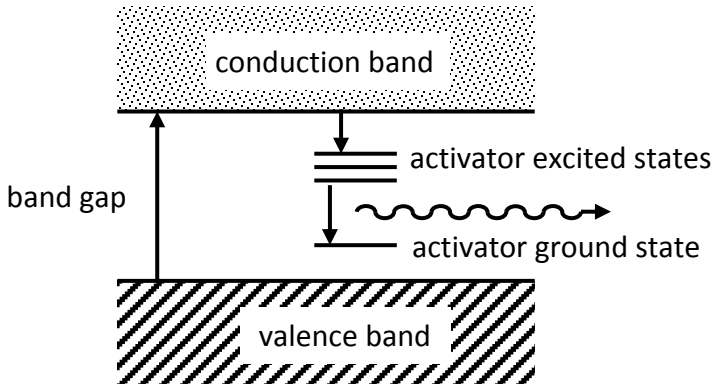

Figure 8. Illustration of energy bands in an inorganic scintillator with activator. Straight-lined arrows indicate electron excitation and de-excitation within the various energy bands. Based on Knoll, 2000 [15].

These light-producing processes give each different scintillator material a characteristic "decay time", which is defined in (2):

$$I = I_0\left(e^{-t/\tau} - e^{-t/\tau_1}\right), \tag{2}$$

where I is the intensity as a function of time t, I_0 is the initial intensity, τ is the decay time, and τ_1 is the characteristic time required to excite the electrons to the conduction band, or rise time. The decay time is important for determining the values of the preamplifier components, to either improve the energy resolution or decrease the amount of pulse pile-up [15].

2.2. Solid-State Photomultipliers

2.2.1. History

The development toward SSPMs started at RCA and at Shockley Laboratory in the early 1960s with experiments aimed at developing avalanche photodiodes (APDs) [20] [21] for the detection of single photons. Various developments led to arrays of APDs from Rockwell International Science Center in 1987 [22] and Radiation Monitoring Devices [23] in 1999. A particular variant of the APD comprised of a metal-resistor-semiconductor (MRS) structure. The metal was typically a very thin layer of titanium, so as to attenuate as few photons as possible, and the resistor a transparent silicon carbide or oxide [24]. These arrays of MRS APDs were developed into arrays of Geiger-APDs (GAPDs), or what is herein referred to as a SSPM [22]. An example of GAPD structure is shown in figure 9.

Other sources use “SSPM” for a slightly different class of devices [22]. Still others call the device used in this work a “silicon photomultiplier” or “multi-pixel photon counter” [25] [26]. The type of device used in this work is referred to as a SSPM for two reasons: 1) they are the effective alternative for PMTs [27] [28] and keeping a similar name highlights this relationship between the devices, and 2) these devices can theoretically be made from different semiconductor materials [29] [30]. There is a multitude of devices, present and future, that thus conform to the “SSPM” description; their differences are largely irrelevant in this chapter and the specifications of the devices used in this work can be found in chapter three.

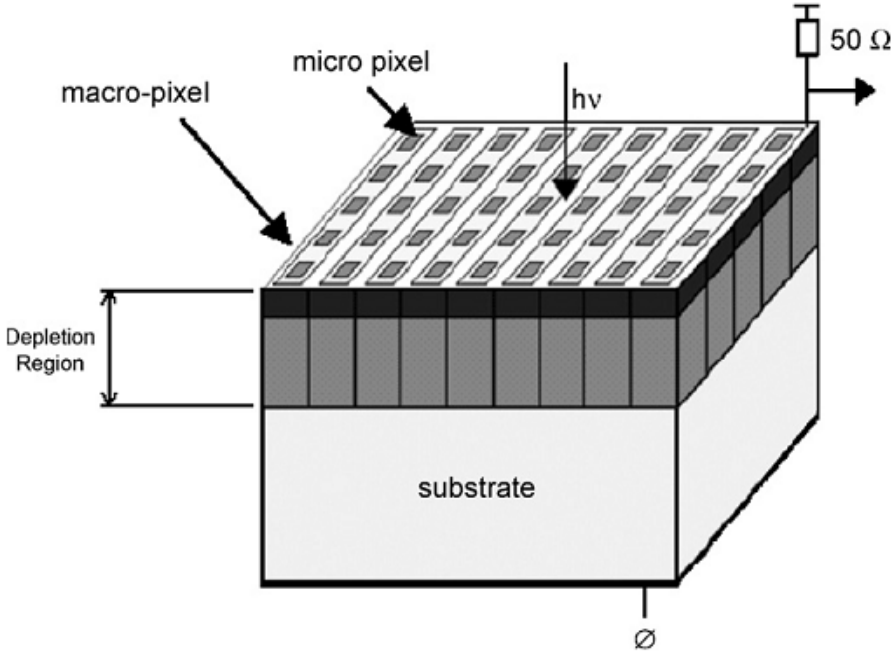

Figure 9. General physical structure of a GAPD, taken from M McClish, *et al.*, 2007 [31].

2.2.2. Principle of Operation

SSPMs consist of a number of "microcells", which each consist of the MRS structure described above. The exposed outer surface of these microcells comprises the light-sensitive area of the SSPM. Between these microcells is an opaque material which reduces cross-talk, or photons generated in a discharge that travel to a neighboring microcell. The metal/resistor side of each microcell is connected to a common anode, and the semiconductor side is connected to a common cathode. The SSPM is reverse biased, so a positive voltage is applied to the cathode. A schematic illustration of the SSPM structure is shown in figure 10. The amplitude of the individual Geiger discharges depends on the magnitude of

the applied voltage bias, and the capacitance and breakdown voltage of the microcells [22] [32].

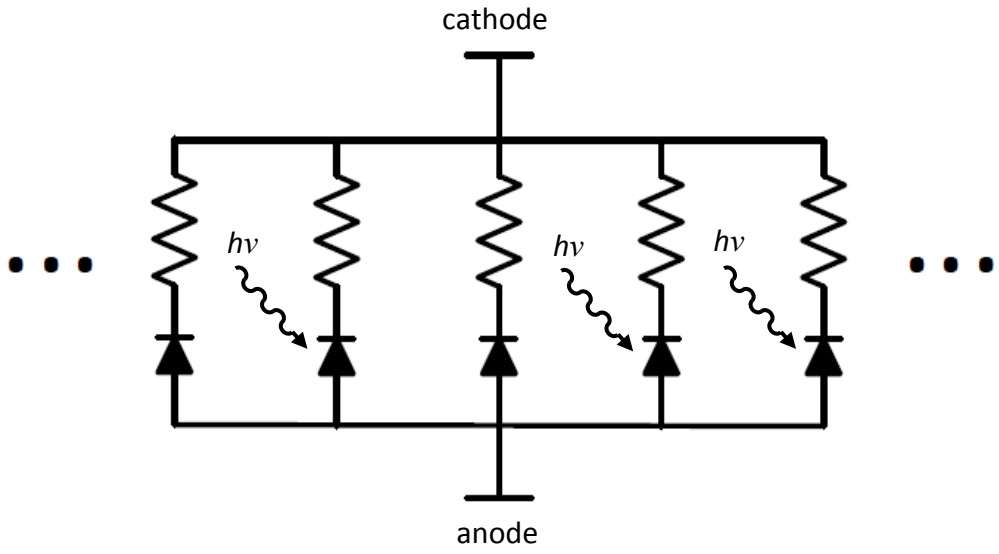

Figure 10. Illustration of SSPM electrical schematic. Each resistor-diode pair represents one microcell. The dots on either side indicate that additional microcells beyond the number shown in the figure may be present. Based on Introduction to the SPM, SensL [32].

SSPMs operate on the principle of Geiger discharges, similar to that of a Geiger-Müller (GM) tube [15] [33]. When a photon incident on the SSPM successfully interacts and creates an electron-hole pair (EHP), the electron is accelerated across the electric field of the microcell, creating more EHPs to form a Geiger avalanche. Thus, the microcell will discharge with approximately the same current every time it is triggered. The Geiger avalanche is quenched when the current across the resistor in each microcell triggered increases, increasing the voltage across the resistor and decreasing the voltage across the diode. When the voltage is reduced below the breakdown threshold, the avalanche is

quenched and the voltage is charged back to its original setting based on the resistance and capacitance of the microcell. A SSPM can have tens of thousands of microcells in a few square millimeters of “sensitive area”. Ideally, when scintillation light is incident on this sensitive area, each photon will be absorbed in a different microcell, making the number of microcell discharges proportional to the number of scintillation photons. This means that the amount of charge induced on the common anode will be proportional to the energy deposited in the scintillator. SSPMs can thus be used for spectroscopy, and not only detection as with a GM tube [22] [32].

However, photons are not always absorbed in different microcells in real devices. Because the microcells produce Geiger-discharges when triggered, if two or more photons are absorbed in the same microcell at the same time, the microcell still responds as if only one photon was absorbed. This phenomenon is called saturation and is intrinsic to all SSPMs. The saturation of a SSPM can be approximated by (3) [34]:

$$N_{fired} = M \times \left(1 - \exp\left(- \frac{PDE \times N_{ph}}{M} \right) \right), \tag{3}$$

where N_{fired} is the number of microcells triggered, M is the maximum number of microcells, PDE is the photon detection efficiency, and N_{ph} is the number of photons incident on the sensitive area of the SSPM at a given instant. The number of photons incident on the sensitive area of the SSPM is dependent on the energy of the radiation and the light yield of the attached scintillator.

SSPMs, being semiconductor devices, are highly dependent on temperature [35] [36], which causes spontaneous excitation of electrons in the crystal lattice across the band gap [37]. Changes in temperature during measurement can result in broadening of full-energy peaks, and thus degrade energy resolution.

2.3. Digital Processing Techniques

A conventional analog pulse processing chain may consist of a number of different components, including preamplifier, shaping amplifier, single channel analyzer, pile-up rejector and peak detector, to name a few [38]. The objective of a digital processing system is to encompass as many of these components in the digital domain as possible in order to reduce the number of physical components in a given system, thus making it more compact. This also reduces a system's dependency on temperature and noise since digital systems use voltage thresholds instead of continuous values. A diagram of a sample analog system and digital system are illustrated in figure 11.

Some components, such as the preamplifier, are still used in digital processing systems, though not necessarily [38] [39] [40]. An example of a digital processing chain would be a preamplifier, ADC, and FPGA. In this case, the pulses from the preamplifier are digitized by the ADC and transferred to the FPGA. All other components, such as triggers, multi-channel analyzers, and oscilloscopes are implemented in hardware code. This both simplifies the hardware and allows the digital processing in the FPGA to be reconfigured simply by reprogramming the device, which affords a high degree of flexibility for the device. Even events that

normally cause problems in performing spectroscopy, such as pile-up peaks, can be dealt with as appropriate in the digital realm [41].

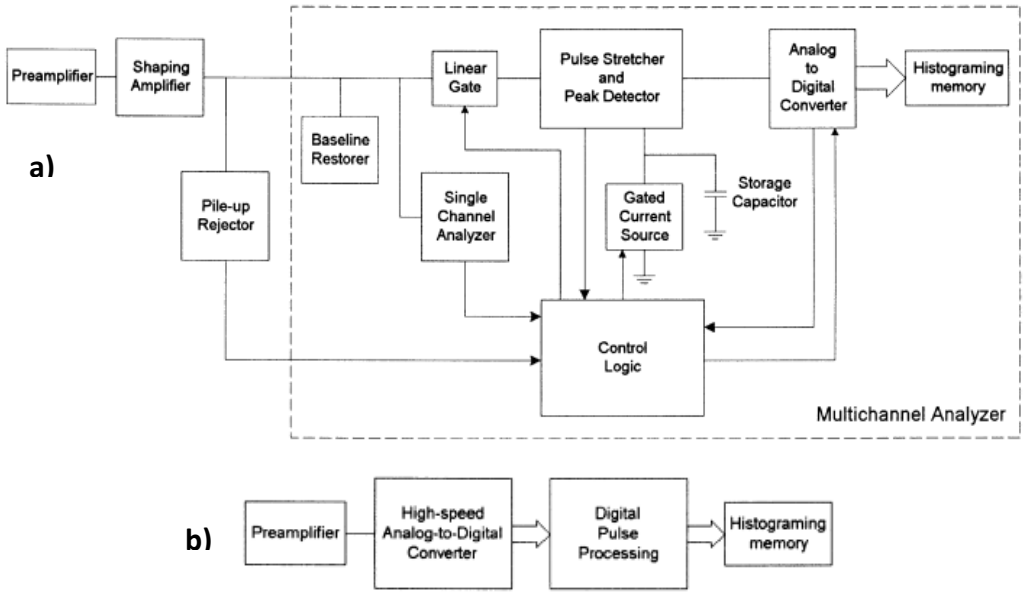

Figure 11. Examples of a) an analog pulse processing chain, and b) of a digital pulse processing chain. Both taken from Simoes, 1999 [38].

3. MATERIALS AND METHODS

3.1. Miniature Spectrometer

The Miniature Spectrometer, or “MiniSpec”, is designed as a gamma spectrometry device that possesses three key features:

- self-contained: everything aside from the user interface should be encompassed in the physical spectrometer itself;
- wireless: the spectrometer should be able to communicate to and display data on most wireless devices that support a graphical user interface;
- marketable: the spectrometer should appeal to individuals and organizations through high-mobility, cost-effectiveness, long device life using a commonly available battery, and small size.

These features were implemented in the MiniSpec prototype by designing a printed circuit board (PCB) that accommodates the detector, analog conditioning electronics, FPGA-based digital pulse processor (DPP), temperature sensor, and power regulators. The PCB with all mounted components is also referred to as the “spectrometer module”. A mobile phone battery can be connected to the detector module to provide power and a small wireless network card can be plugged into a header on the detector module connected directly to the FPGA to provide wireless connection options. A schematic representation of the overall system design is shown in figure 12.

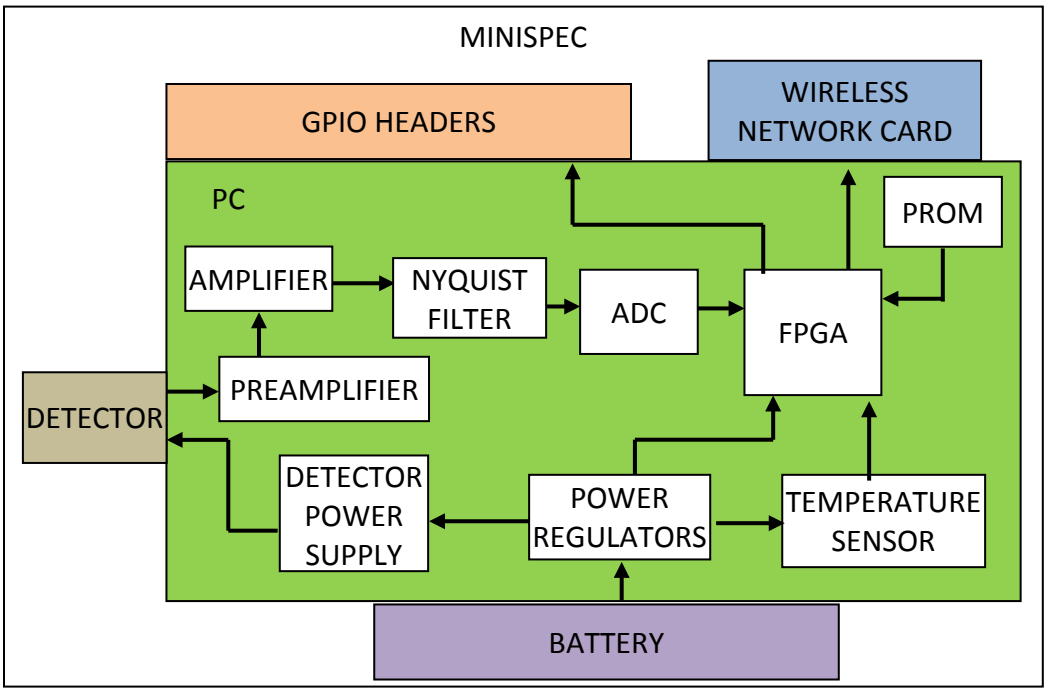

Figure 12. Diagram of the components comprising the complete MiniSpec system.

3.2. MiniSpec Design

3.2.1. Detector

The radiation detector is composed of a SSPM and optically-coupled CsI(Tl) crystal wrapped in white Teflon tape and enclosed in a custom light shield. The CsI(Tl) crystal is 6x6x10 mm, and was procured from Hilger Crystals, Inc. [42] with a reflective coating already applied to all but one of the 6x6 mm faces. The SSPM is a MicroSL 60035 model from SensL [43].

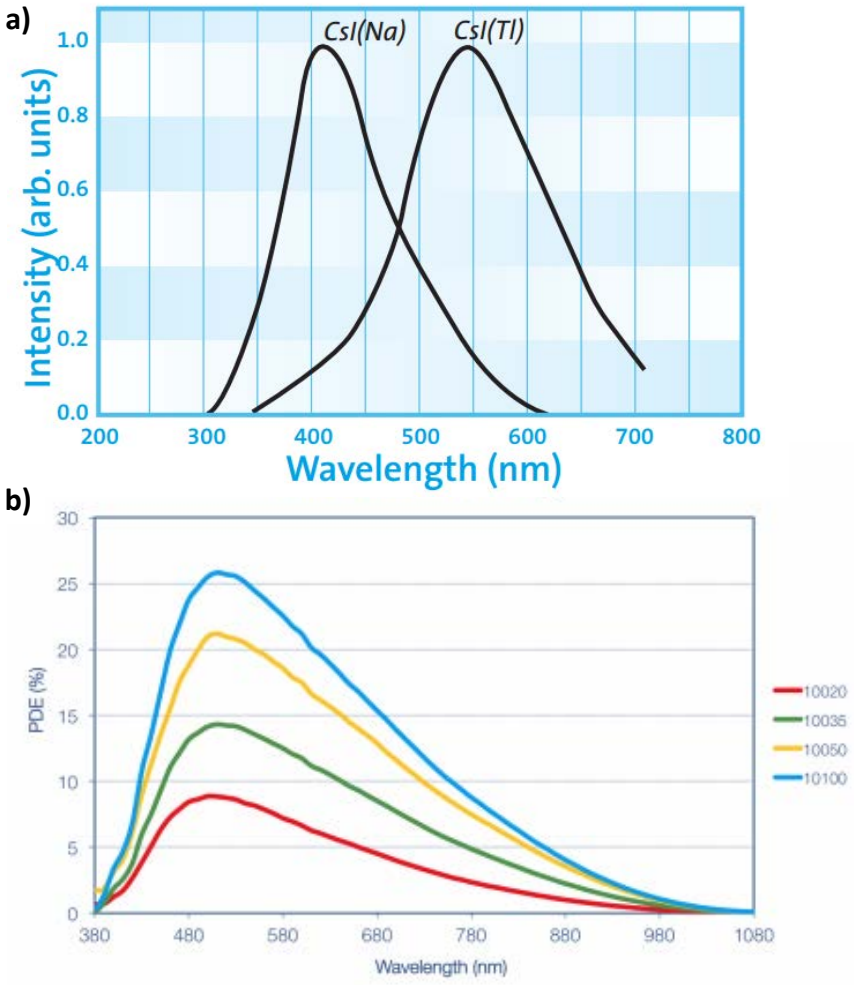

Figure 13. Illustrations of a) CsI(Tl) light yield for different wavelengths (taken from Saint-Gobain CsI datasheet) [44], and 2) SSPM PDE at different wavelengths for different devices; the SSPM used in the MiniSpec follows the green, 10035 line (taken from SensL MicroSL datasheet) [43].

CsI(Tl) is relatively well-suited for use with the MicroSL device. The wavelength at which the most light is generated in CsI(Tl) varies with the amount of thallium doping [45], but is generally between 500 and 565 nm, as shown in figure 13a. The crystal used in the MiniSpec is specified to have a peak light output wavelength of 565 nm [42]. The SSPM has peak photon wavelength sensitivity at

500 nm, but maintains relatively high photon detection efficiency (PDE) at 565 nm [43], as shown in figure 13b as the green, 10035 line. The SSPM and CsI(Tl) crystal were coupled using BC-630 optical grease to facilitate light transmission from the crystal to the photosensitive area of the SSPM. Specifications for the SSPM [43] and CsI(Tl) [42] are given in tables 1 and 2.

Table 1. SSPM specifications.

SSPM parameter	**value**
breakdown voltage	27.5 V
recommended operating voltage	29.5 V
number of microcells	19096
PDE at peak sensitivity	14%
gain	2.4×10^6
dark current	12.0 μA
temperature coefficient	21 mV/°C
cross-talk probability	21%

Table 2. CsI(Tl) specifications.

CsI(Tl) parameter	**value**
decay constant	1.0 μs
peak scintillation wavelength	565 nm
photons/MeV	52,000

The assembly was then wrapped in Teflon tape to reflect light internally, to help shield outside light, and to help keep the two parts together. The assembly was

then placed inside a custom light shield made from cut pieces of molded plastic and black electrical tape, with orange electrical tape used to hold the bottom cover in place and to indicate the cathode side of the assembly. The effectiveness of this light shield was verified by monitoring the SSPM output on an oscilloscope while toggling the room lights on and off. The separate SSPM and CsI(Tl), the wrapped assembly, and the assembly covered by the light shield can be seen in figure 14.

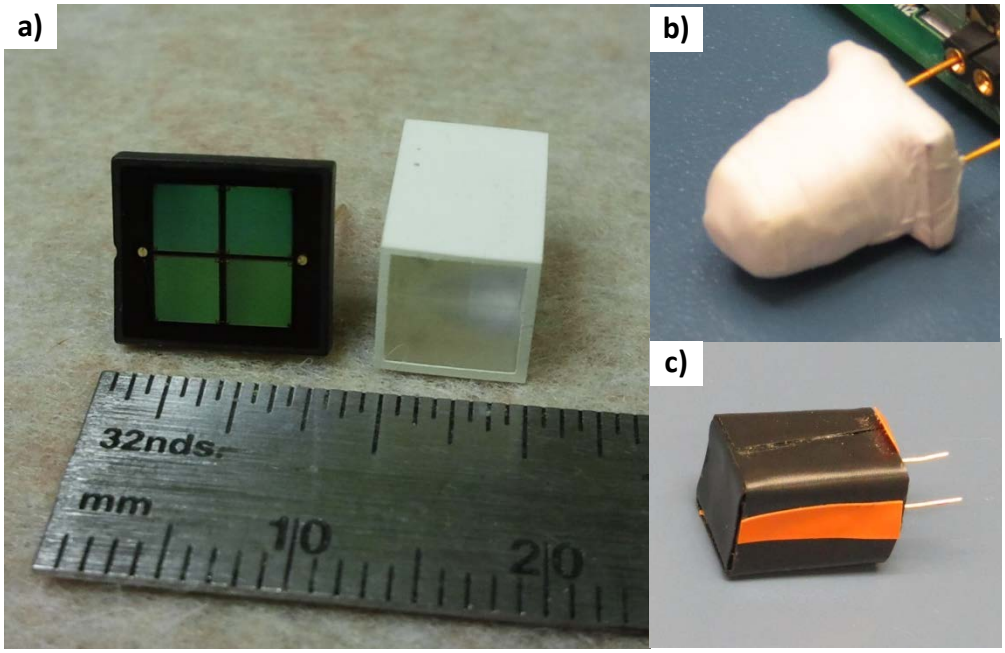

Figure 14. Pictures of a) the SSPM (left) and reflectively-coated CsI(Tl) crystal (right), b) the coupled crystal and SSPM assembly wrapped in Teflon tape, and c) the assembly inside the custom light shield.

This detector is relatively small, approximately 3.528 cm^3 including the CsI(Tl) crystal, SSPM, reflective covering, and light shield. CsI(Tl) also has a relatively high average atomic number which, as previously discussed, is better-suited to

detecting gamma rays [17]. The SSPM has several advantages over the more common PMT, which include its smaller size, lower bias voltage, insensitivity to magnetic fields, and better durability [27] [28]. All of these qualities are desirable for a device designed for use outside a controlled laboratory environment.

However, one major disadvantage of using a SSPM is its sensitivity to temperature [22] [34]. The breakdown voltage of the MicroSL has a reported temperature dependence of 21mV/°C [43]. If the operating voltage is kept constant, the amount of over-voltage will decrease as temperature increases, decreasing the performance of the detector. Thus, for a mobile device, a temperature-correction algorithm should be implemented to keep the device at optimum performance. This is addressed later in section 3.2.4.

3.2.2. Analog Conditioning

The analog conditioning electronics on the detector module consist of a charge-sensitive preamplifier, inverting gain stage, and a 2^{nd}-order RLC filter and differential signaling stage, shown in figure 15.

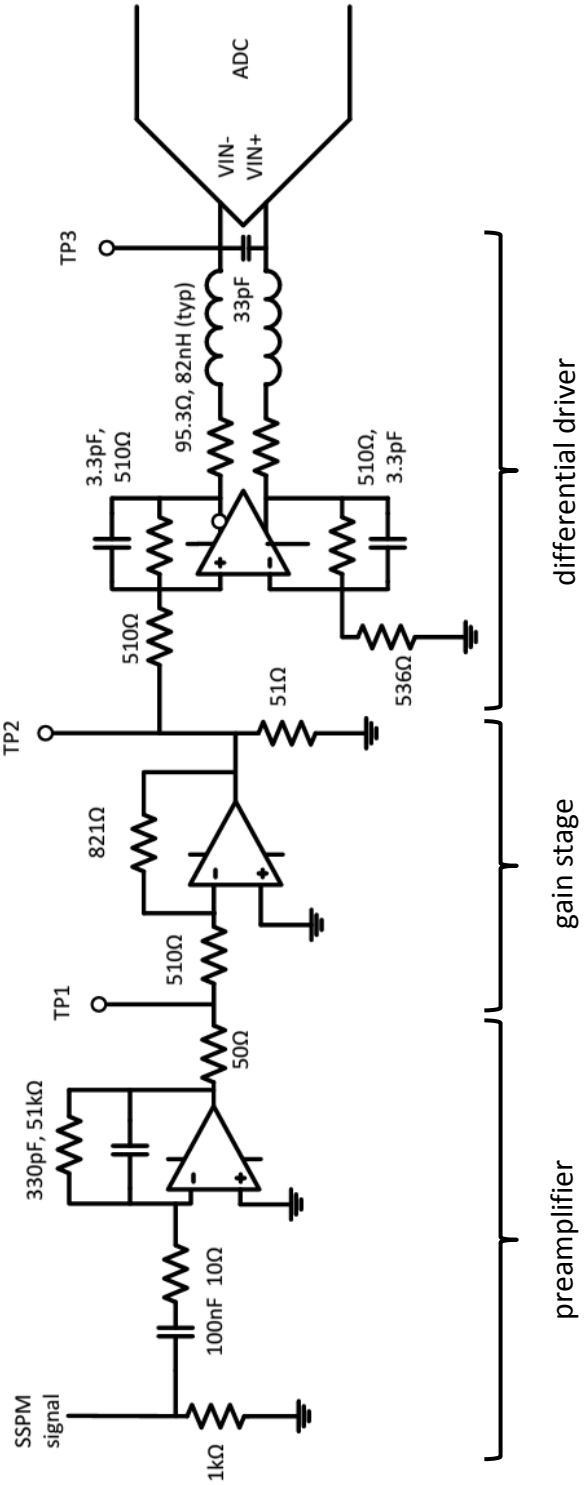

Figure 15. Schematic of the analog processing chain with labeled test points.

The charge-sensitive preamplifier is required for proper readout of the SSPM since it is a semiconductor device. The preamplifier integrates the change produced by the SSPM, generating an output pulse the amplitude of which is proportional to the energy absorbed in the CsI(Tl) [15]. A fast (non-charge sensitive) preamplifier was used in previous experiments involving this device and is believed to have contributed to the poorer-than-expected energy resolution of the acquired spectra [46]. The operational amplifier (op amp) used in this stage was the OPA656 from Texas Instruments [47].

The choice of capacitor value is based on the maximum expected charge that can be generated by the SSPM, based on (4):

$$Q_{\max} = q_e \times N_{cells} \times G_{cell}\,, \tag{4}$$

where Q_{max} is the maximum charge, q_e is the charge of one electron ($1.602\text{x}10^{-19}$ C), N_{cells} is the number of microcells in the device (19096), and G_{cell} is the gain of an individual microcell ($2.4\text{x}10^{6}$) [43]. Given the values for the MicroSL device used, the maximum charge possible was calculated to be 7.34 nC. However, the actual maximum was assumed to be 1.0 nC based on manufacturer recommendation (private conversation with SensL). With the capacitor value of 330 pF, this yields a 3.03 V maximum signal amplitude.

The time-constant of the preamplifier is equal to the product of the resistance and capacitance of the feedback components. These two values determine the circuit's time constant, also commonly referred to as the "RC constant". It is important for this constant to be much larger than the decay time of the

scintillator in order for the amplitude of the resulting pulse integration to be proportional to the energy deposited in the radiation interaction [15]. The decay time of CsI(Tl) is commonly held to be approximately 1000 ns [42] [48] [49], though in actuality it possesses two different, superimposed decay times [15]. Thus, and also at the recommendation of SensL, the resistor value was chosen to be 51 kΩ in order to obtain a time constant of 17 μs [50].

The gain stage allows for tuning of the peak signal voltage in order to cover the entirety of the digital pulse processor's 2.0 V peak-to-peak dynamic range, yielding the best digital resolution for the desired gamma energy range. The gain stage also inverts the preamplifier signal. The preamplifier pulses have negative polarity, so the output of the gain stage will have positive polarity. The gain of this stage can be calculated using (5) [51]:

$$G = -\frac{R_2}{R_1}, \tag{5}$$

where G is the gain, R_2 is the value of the resistor connected between the inverting input and output of the op amp, and R_1 is the value of the resistor connected between the incoming signal and the inverting input. The values used in the MiniSpec prototype are R_1 = 510 Ω and R_2 = 821 Ω, as seen in figure 15, resulting in G ≈ -1.61. The op amp used in this stage was the OPA847 [52].

The RLC filter, shown schematically in figure 16 for single-ended signals, damps frequency components of the signal that are greater than the Nyquist frequency,

or half the sampling frequency of the ADC, and is based on a commercial filter [53].

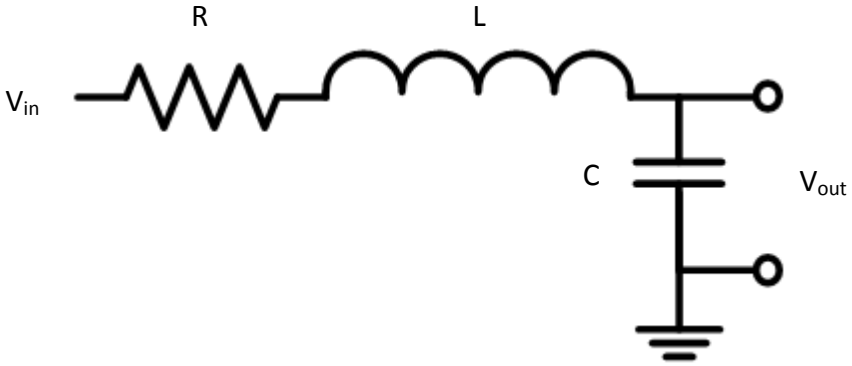

Figure 16. RLC circuit diagram used for Nyquist filter into the ADC.

Finally, the differential signaling stage transforms the single-ended signal from the previous stages into a differential signal for input to the ADC. This is done by using an Analog Devices AD8138 [54] with a single-ended input. The RLC filter discussed above is incorporated into the differential output, based on a commercial design [53].

3.2.3. Digital Pulse Processor

The DPP, illustrated in figure 17, consists primarily of an ADC and FPGA, with other digital peripherals connected to the FPGA, such as the CMOS oscillator and temperature sensor.

The ADC is the Analog Devices AD9629-40 [55], which has a maximum sampling frequency of 40 MHz and has 12-bit resolution, with a 2.0 V peak-to-peak input dynamic range. The AD9629 is available in four different models all

corresponding to a different sampling frequency, but all with the same device package. Thus, if a higher sampling rate is required, for example in the case of a scintillator with a faster characteristic decay time, the same PCB may be used with an AD9629 model with a higher sampling frequency. The ADC transfers the digitized differential signal to the FPGA, a Xilinx Spartan 6 [56]. The FPGA connects to three GPIO headers on the detector module, one of which is specifically configured to allow for connection to the Flyport wireless network card.

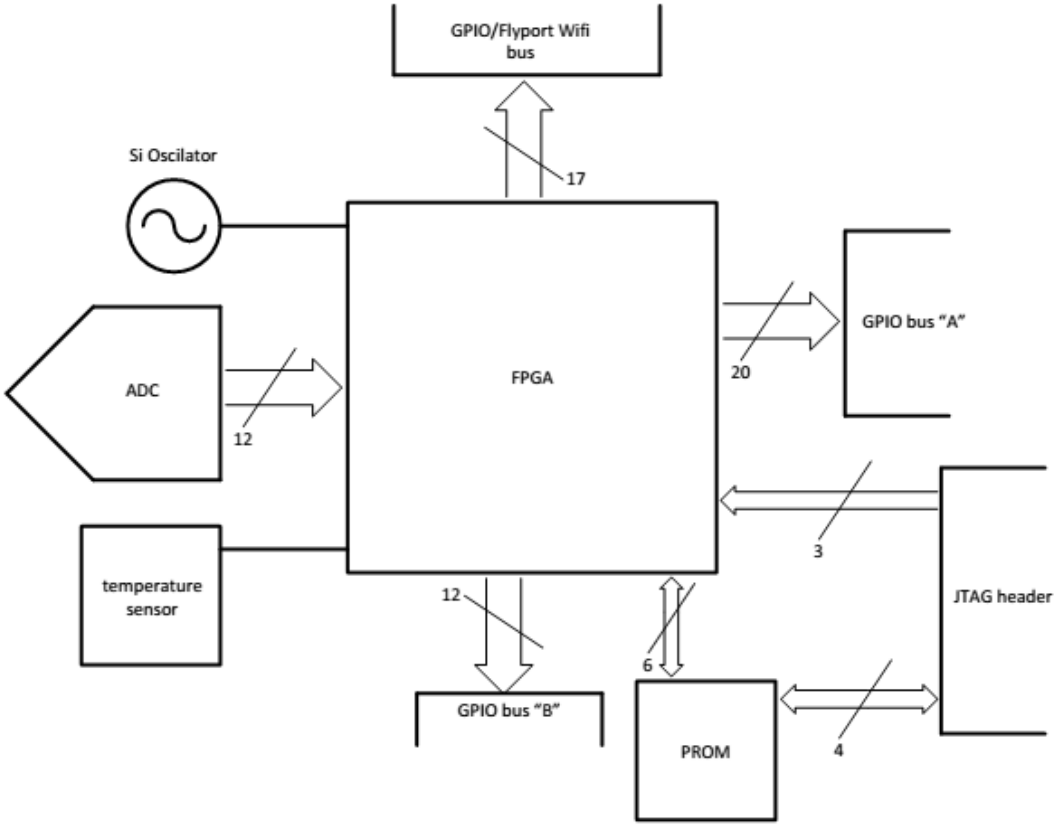

Figure 17. Schematic of digital pulse processor and peripherals.

The FPGA can be programmed either via Xilinx Platform Cable USB II device or 4 Mb programmable read-only memory (PROM) chip. Both the FPGA and PROM are included in the JTAG programming chain on the spectrometer module [57]. When the FPGA is powered up, if the PROM has previously been loaded with a compatible bit-file, the FPGA will automatically be programmed using this file. This allows the FPGA to retain its functionality after being turned off and then back on, essential for use outside laboratory environments and without JTAG programming equipment at hand. The FPGA may also be programmed with a compatible bit file directly via the JTAG header.

The FPGA is also responsible for managing all clocking inputs and outputs. The detector module has an on-board 20 MHz silicon oscillator [58] connected to the FPGA. The FPGA synthesizes this input to a 40 MHz clock using an internal digital clock manager (DCM), and uses a differential output buffer to send this clock to the differential ADC clock inputs. The ADC digital clock output (DCO) is also connected to the FPGA as an input, which is also routed through a DCM for enhancing the timing performance of the FPGA firmware, such as defining setup and hold times, and used as the main clock for the digital processing algorithm.

The pulse processing algorithm possesses two parts: an oscilloscope mode and a MCA mode, both developed previously by Dr. Abi Farsoni. Both modes rely on a trigger module to be notified of an incoming, valid pulse. The trigger module is based on a triangular finite impulse response filter, the output of which is compared to a user- or pre-defined threshold. If a valid pulse arrives, the trigger will send a “one-shot”, or one clock-cycle, output to both the oscilloscope and

MCA modules, only one of which will activate depending on which mode the device is set to.

In oscilloscope mode, a valid pulse signal from the trigger module begins the process of saving each successive incoming ADC sample to a write-first circular buffer with 2048 addresses of 16 bits each. Port A on this buffer is set by the 40 MHz system clock. This port is only used for writing data to successive addresses, controlled by a counter. Port B is set by the host clock when connected to the Opal Kelly USB interface board, discussed in section 3.2.6.

In MCA mode, a valid trigger pulse begins the process of sampling the maximum of the pulse, which is proportional to the energy of the interaction, and incrementing the appropriate address in a dual-port, write-first Block RAM with 4096 addresses of 32 bits each. Before sampling, the pulses are shaped by a recursive digital trapezoidal filter, developed by Dr. Abi Farsoni. The trapezoidal filter both enhances the signal-to-noise ratio and reduces the number of pileup events in the system [59].

Sampling the maximum of a pulse from a charge-sensitive preamplifier can be performed in several ways, including a sample-and-hold circuit [60] or a digital peak-finding algorithm [61]. In the MiniSpec, the rise and fall time of the filter and analog circuit pulses are known, so the convolution of the two pulses (the output) can be sampled in the same temporal location for every pulse to obtain the proportional value. The sampling location in the MiniSpec was set to the sum of the peaking and flat times. The sampled amplitude is converted into a histogram address, which is then incremented and the process repeated. The

histogram that is generated in the Block RAM is accessed in the same manner as the circular buffer of the oscilloscope module.

3.2.4. Temperature Sensor

As previously discussed, solid-state devices such as the SSPM are sensitive to temperature. Since the MiniSpec is intended to be used outside controlled environments, being able to correct for anticipated changes in temperature is crucial to proper operation of the device. Thus, the Maxim DS1822 temperature sensor [62] has been included in the spectrometer module. It uses a one-wire interface with the FPGA, which combines power and communication in one connection. The maximum temperature resolution of the device is 0.0625 °C, which, given the SSPM bias sensitivity of 21mV/°C, means that a bias change of approximately 1.31 mV can be detected.

This information provided by the temperature sensor was intended for use in a correction algorithm in the FPGA to adjust the gain of the recorded pulses. However, this aspect of the project was unable to be completed in time and is not included here.

3.2.5. Power Supply

Various components on the detector module require different voltages for proper functionality. A total of six voltage regulators ultimately provide the seven voltages necessary to power the SSPM and the various integrated circuits on the detector module. The power supply chain is shown in figure 18.

The 3.7 V rail, generated by fixed power supply or mobile phone battery, is converted to the biasing rail for the SSPM by a MAX5026 step-up DC-DC converter [63]. This voltage is made adjustable from 28.7 – 29.5 V to accommodate the slight difference in optimal bias voltages between SSPMs. This was accomplished by incorporating a trimmer potentiometer into the feedback resistor layout of the MAX5026 itself.

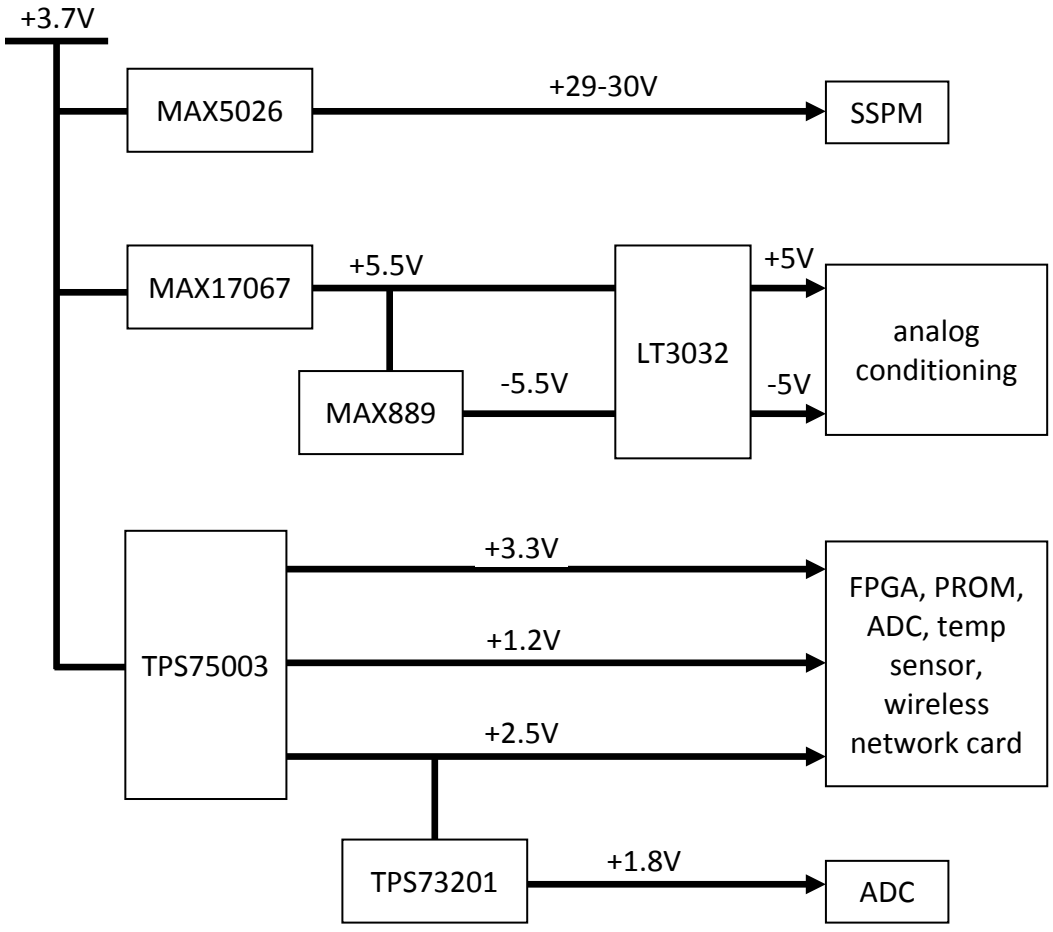

Figure 18. Diagram of power distribution on the detector module.

The 3.7 V supply is also converted into 5.5 V by a MAX17067 step-up DC-DC converter [64]. This is then routed to a MAX889 inverting charge pump [65] to provide -5.5 V. These two voltages are then used as inputs to the LT3032 linear regulator [66], which outputs low-noise ±5 V power for the analog conditioning section.

Finally, the 3.7 V supply is routed into a single regulator, the TPS75003 [67], that provides all three of the voltages required by the FPGA. The 3.3 V and 1.2 V rails are generated by switching supplies since they do not need to be low-noise. The 2.5 V supply is provided by a linear regulator in the TPS75003, and also routed through the TPS73201 linear regulator [68] to supply the 1.8V analog power for the ADC.

The power consumed by the fully-functional system was measured using a multi-meter connected in series with the power input of the MiniSpec. The amount of current drawn was 300 mA, making the power consumption 1.11 W. A typical smart mobile phone battery has about 600 – 700 mA-h of power, which could power the MiniSpec for about two hours. Smart phone batteries with larger mA-h ratings are available, and would be able to power the MiniSpec for longer.

3.2.6. USB Interface Board

Before accessing the MiniSpec via its Flyport wireless interface, a separate USB interface board was used to verify the functionality of the MiniSpec and save spectra for analysis. The Opal Kelly XEM6001 [69] was used for this purpose. As well as a USB port and a Spartan 6 FPGA, the XEM6001 features three GPIO

headers for communicating with other devices. The XEM6001 can be programmed and communicated with using a MATLAB [70] script via the USB interface.

The Opal Kelly “Host Interface” (HI) hardware code was implemented between the XEM6001 and the FPGA on the detector module. This code is provided by Opal Kelly, and serves as means of communication between the USB port and the FPGA. The HI can be depicted as shown in figure 19.

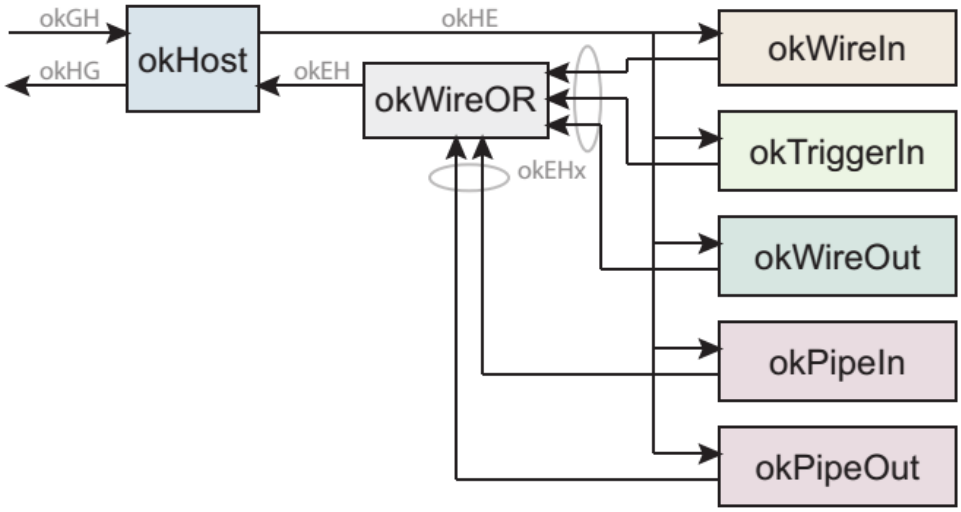

Figure 19. Diagram of Opal Kelly host interface components and connections, taken from Opal Kelly FrontPanel User Manual, 2012 [71]. Used with permission.

Input commands and data are sent using MATLAB. The HI reads these commands and data, and routes them to certain “endpoints”, based on the type of signal and a unique address. The original input signals can then be read from these endpoints in the FPGA hardware code [71]. Normally, the HI and endpoints are implemented on the XEM6001. However, because the detector module has a

limited number of GPIO pins, only the HI was implemented on the XEM6001. The signals connecting the HI to the endpoints (okHE and okEH in figure 19) were instead routed to the GPIO headers on the XEM6001. These headers were connected to the GPIO headers on the detector module, and the endpoints implemented on the FPGA on the detector module.

3.2.7. Wireless Interface

The Flyport wireless network card (Flyport) [72] can plug directly into a header on the PCB, which is connected directly to the FPGA. The Flyport has two modes of operation: “infrastructure” and “ad-hoc”. In infrastructure mode, the Flyport connects to an existing wireless network. In ad-hoc mode, the Flyport generates a wireless network that other devices may connect to and use to access the module [72]. Ad-hoc mode is ideal for MiniSpec since a wireless network may not be available when a user wishes to use the device. When this is the case, the ad-hoc mode allows any wireless-capable device, such as a mobile phone, to connect to the wireless network generated by the Flyport.

The Flyport was unable to be fully implemented in the MiniSpec due to time constraints. Values from the FPGA were successfully written to the Flyport, and successfully transferred to the webpage on the client, but a complete system that would allow the user to view the histogram on the client was not completed.

3.2.8. PCB Design

The spectrometer module PCB was designed to include all power regulators, the analog conditioning chain, digital pulse processor, and peripheral connections, such as battery power header, GPIO headers, Flyport -compatible header, and detector sockets. Because of the number of voltages on-board and the close proximity of the components requiring different voltages, six layers were used: the top and bottom for surface-mount components, the first inner layer for the ground plane, and the other three inner layers for various voltage planes. Figure 20 shows the finished but unpopulated PCB for the MiniSpec. The PCB was designed using PCB123 software [73]. The PCB was manufactured at Sunstone Circuits [74] and assembled at Screaming Circuits [75].

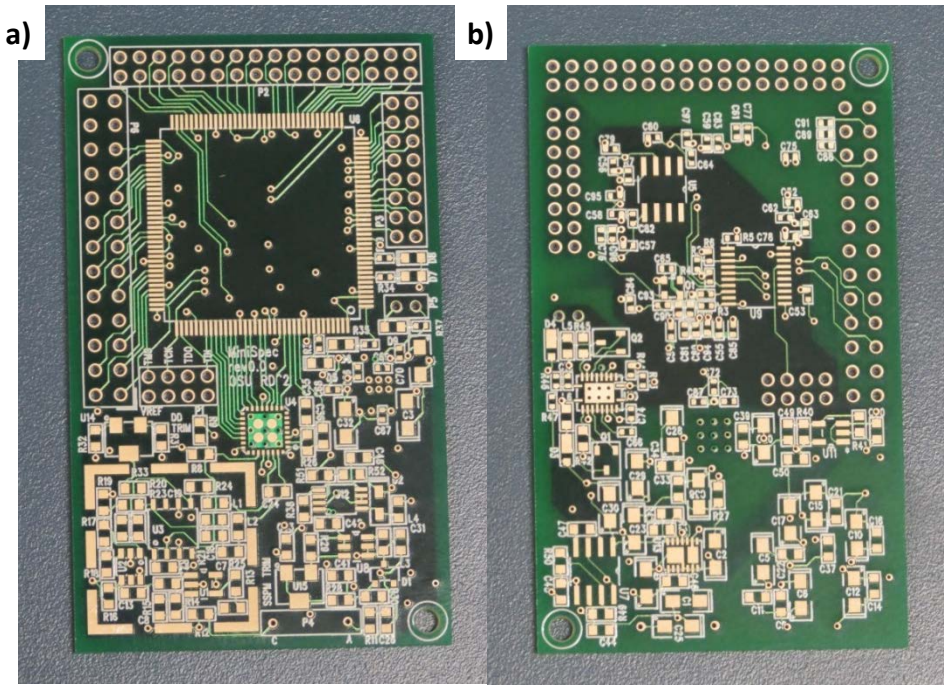

Figure 20. MiniSpec PCB a) top, and b) bottom.

Because the analog, digital, and power regulation sections of the detector module design are all included on the same board, mixed-signal design features were implemented. For all devices, a number of de-coupling capacitors were connected between the traces carrying power and the ground plane, the number and values of which depended on the device. The analog section was also covered by a RF shield connected to ground. The analog and digital sections were also separated and the ground plane only connected at the two-pin power header to form a star-ground, which reduces noise from ground loop currents [76] [77].

3.2.9. Cost

A major consideration when designing the MiniSpec was cost. As mentioned in section 3.1, cost-effectiveness is an aspect of marketability that is essential to any possible commercialization of MiniSpec. The total cost of the MiniSpec prototype was approximately $1089: the SSPM was approximately $200, the CsI(Tl) crystal was $65, the Flyport was about $52, and each PCB was approximately $60 for manufacture, about $563 to assemble, and the parts for each of the two boards assembled were $149 per board.

However, because a relatively low number of components were purchased, this composite cost is not reflective of the final mass-production cost. Bulk orders of the SSPM and CsI(Tl) crystal, for instance, could cost as little as $30 (private conversation with SensL) and $12 (private conversation with Hilger Crystals) per item, respectively. It is estimated that a commercial version of the MiniSpec would cost $150 or less, including hardware costs and firmware development

costs. For comparison, other handheld devices, such as the ICS-4000 [78] and rad-ID [79], range from $9,475 to $19,995 [80]. In addition, these devices are up to 7295 cm^3 in volume, and weigh up to 7 lbs., whereas the MiniSpec could be as small as 250 cm^3, and weigh as little as 12 oz.

3.3. Radioactive Sources

Six different button sources from Spectrum Techniques [81] were used to generate spectra using the MiniSpec: ^{109}Cd, ^{137}Cs, ^{57}Co, ^{60}Co, ^{54}Mn, and ^{22}Na. All isotopes were calibrated to 1 μCi on March 05, 2012 with 15% error.

3.4. MCNP Modeling

MCNP5 [82] was used to model the CsI(Tl) crystal as a means of checking the results of the efficiency measurements with the MiniSpec. Table 3 shows the list of photon energies simulated and their corresponding isotope of origin. Each one was modeled as a point-source in MCNP. One input deck was generated and run for each energy [83]. The CsI material card used was generated according to a compendium produced by Pacific Northwest National Laboratory [84]. Each deck was run for 10^8 photons, with an energy tally with 1 keV bins in the respective CsI cell of each deck.

These input decks were used to simulate the intrinsic efficiency. Each one consisted of a 10 x 6 x 6 mm CsI right-parallelepiped and an 8.9 x 10.1 x 2.0 mm pure Si right-parallelepiped centered adjacent to the CsI as a model for the CsI(Tl) crystal coupled to the SSPM. In MCNP, the source was positioned on the

axis parallel to the long axis of the CsI, 200 mm from the end of the crystal, mimicking the configuration used for the efficiency measurements, explained in section 3.6. All cells except the CsI and SSPM were set to vacuum. This geometry is illustrated in figure 21 using the VisEd MCNP visualization software.

Table 3. List of energies used in MCNP decks and their corresponding isotopes.

photon energy (keV)	isotope of origin
22.163	^{109}Cd
32.194	^{137}Cs
88.0336	^{109}Cd
122.06065	^{57}Co
511.0	^{22}Na
661.657	^{137}Cs
834.848	^{54}Mn
1173.228	^{60}Co
1274.537	^{22}Na
1332.492	^{60}Co

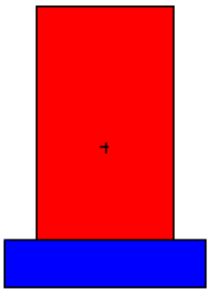

Figure 21. MCNP geometry for the input deck. The source position is not shown.

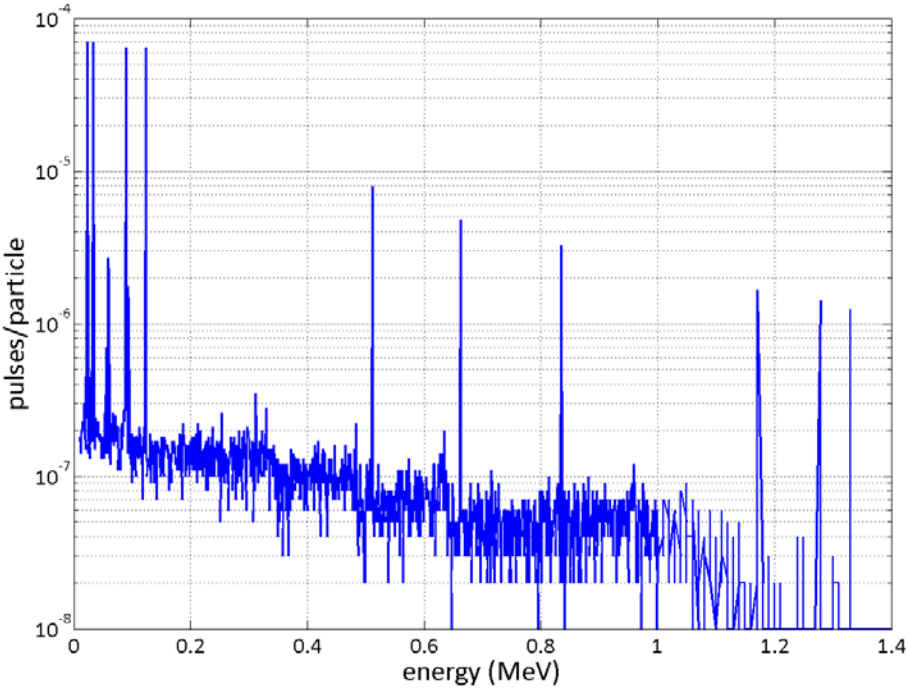

Figure 22. Pulse height tally versus energy plot, a combination of all simulated photon energies.

In figure 22 the pulse height tallies for each photon energy were summed into one tally for simplicity and plotted, and 10^{-8} was added to the number of pulses per particle in each energy bin in order to create a continuous line in log-space. Thus, some of the peaks do not display their true value since they are superimposed over the Compton continuum of higher-energy peaks.

Table 4 shows the intrinsic efficiencies predicted using MCNP for each energy from individual tallies. To obtain the efficiency percentages given in table 4, the pulse height tallies were summed from E – 1 keV to E + 1 keV in each respective

MCNP output, where E is the full-energy peak centroid energy bin. Each sum was then divided by the solid angle subtended by the detector, as discussed in the next section.

Table 4. Intrinsic efficiencies for selected full-energy peaks.

photon energy (keV)	intrinsic photopeak efficiency
22.163	97.77%
32.194	97.33%
88.0336	89.15%
122.06065	88.97%
511.0	11.06%
661.657	6.59%
834.848	4.44%
1173.228	2.30%
1274.537	1.95%
1332.492	1.73%

3.5. Experimental Setups

Two different physical experimental setup configurations were used when taking different sets of measurements. In configuration one, the top of the detector housing was placed against the button source, held upright by a custom-made test apparatus, as shown in figure 23. This configuration was used for all measurements except those used for efficiency calculations in order to obtain the highest number of counts, and therefore achieve adequate statistical robustness for subsequent calculations.

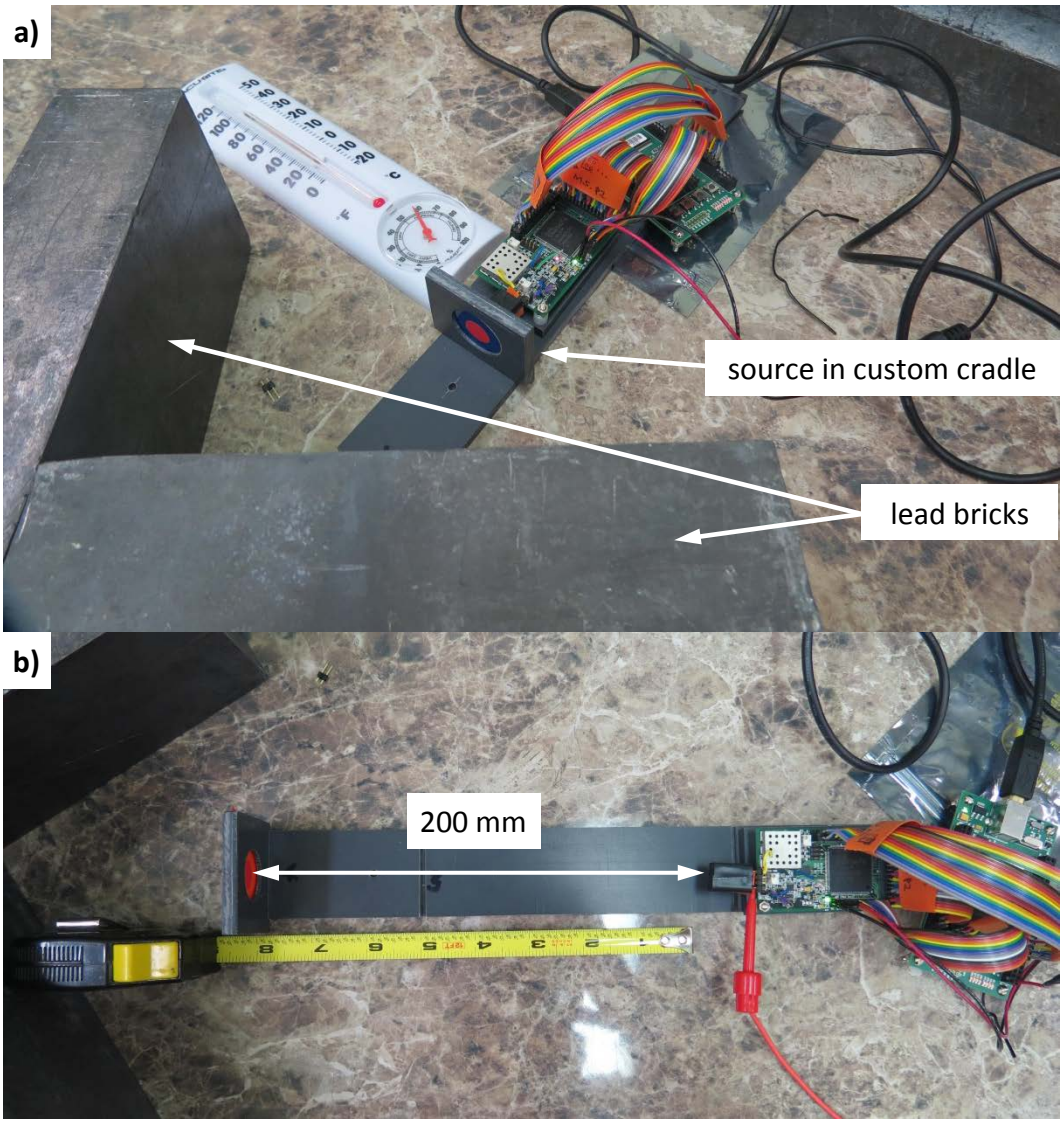

Figure 23. Photographs of a) measurement configuration one and b) measurement configuration two.

In configuration two, also shown in figure 23, a distance of 200 mm was measured between the source and the front of the detector housing. The reason

for this distance was to be able to use the point-source approximation in the efficiency calculations. The solid angle was thus calculated using (6) [15]:

$$\Omega = \frac{A}{d^2}. \tag{6}$$

This approximation requires that *d*, the distance from the source to the face of the detector be much greater than the radius of the detector face. Since the CsI(Tl) crystal has a square face, the radius was approximated as 3.4 mm in order for πr^2 to be approximately equal to the 36 mm^2 of the CsI(Tl) side facing the source. Since 200 mm is almost two orders of magnitude greater than the 3.4 mm "radius", the point-source approximation is appropriate.

Both measurement configurations used two lead bricks to shield laboratory occupants from the radioactive sources measured, in keeping with ALARA dose requirements. All measurements were also set to approximately the same SSPM bias voltage of 29.38 V, though issues with stability are discussed in section 4.1. Six sets of measurements were conducted: a peaking time set, a flat time set, a full-energy peak set, an efficiency set, and a pileup set.

The peaking time is the time during which the trapezoidal filter's coefficients are non-zero, just before the flat section. For the peaking time set, a ^{137}Cs source was measured and the peaking time of the digital trapezoidal shaper was varied between seven different settings while the flat time was held constant, corresponding to 4.5, 7.5, 10, 20, 30, 40, and 50 μs. The spectrum from each measurement was saved and the resolutions compared with one another to find

the optimum peaking time. The same method was used for the flat time set, with the flat time of the trapezoidal filter varied between 0.25, 0.5, 1, 1.5, 2, 2.5, and 3 μs and the peaking time held constant.

The full-energy peak set was used to characterize the linearity, dynamic range, and full-energy peak resolution using the optimum peaking time and flat time found from the previous measurements. The full-energy peaks used for these characterizations are the same as those given in table 1 for the MCNP simulations.

For the efficiency set, experimental setup two was used to characterize the efficiency of the system for the same full-energy peaks as those characterized in the full-energy peak set. Finally, for the pileup set, one each of ^{109}Cd, ^{57}Co, and ^{137}Cs laboratory sources were placed in front of the detector at the same time, and the pileup rejection algorithm in the FPGA turned on and off.

4. RESULTS AND DISCUSSION

4.1. MiniSpec Operational Issues

During the course of testing and bringing the detector module to operational status, a number of issues were encountered. The first category is errors in the PCB design. The nature of these errors varied; some were merely incorrect resistor or capacitor values and some were errors in trace routing. For errors involving incorrect component values, the components were merely replaced with components of the correct value. For trace routing errors, the traces were carefully cut twice with 2 mm of separation with a razor blade, a soldering iron at 720 °F was used to scorch the trace away between the cuts to sever the connection. To connect the correct components together, small wires were soldered to the appropriate pin or solder pads of each component.

The second category was errors that were unable to be corrected. The most important of these was the instability of the SSPM bias voltage. During some measurements, anomalies would appear in the gamma spectrum. In these experiments, it was discovered that the bias voltage of the SSPM had changed during the measurement, changing the gain of the SSPM and resulting in the shift in peak location. This is demonstrated in figure 24.

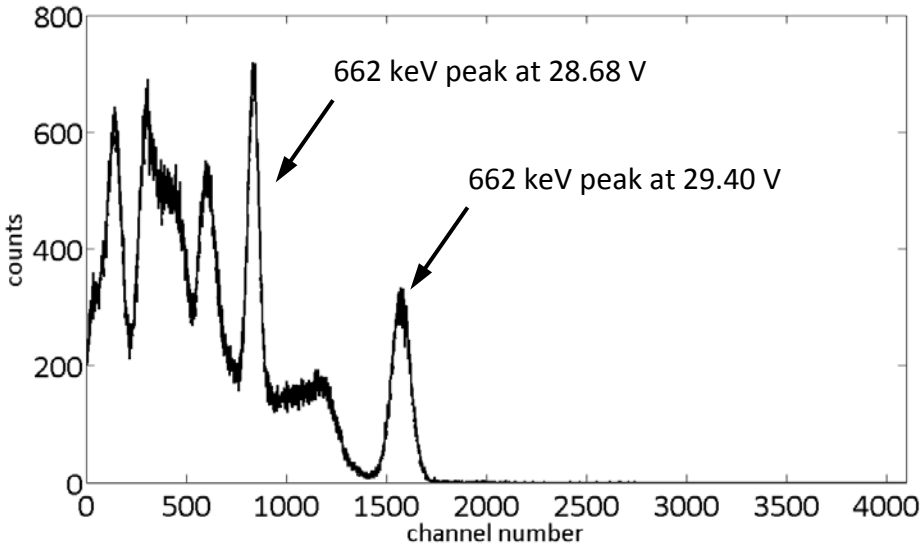

Figure 24. ^{137}Cs spectrum with voltage change from 28.68 V to 29.40 V.

A ^{137}Cs source was placed in front of the detector in configuration one, with the bias voltage set to 28.68 V. After 30 min, the bias voltage was changed to 29.40 V and the measurement continued for another 30 min. As shown in figure 24, the 662 keV full-energy peak shifts by 736 channels. This equates to a shift of about 968 channels per volt, or about nine channels per 10 mV. This can be a significant source of peak distortion and lead to degraded resolution. During measurements, this change in voltage bias is believed to be due to the heating and loss of connectivity between one or more components and their respective PCB pads in the voltage bias circuit. To alleviate this problem, a fan was positioned next to the MiniSpec in an effort to keep these connections cooled and stable.

Figure 25a shows the initial results of a ^{137}Cs energy spectrum measurement as seen in MATLAB: two large spikes between channels 1000 and 1500, one large

spike near channel 4095, and no discernible spectrum. However, when the upper limit of the y-axis is changed, as shown in figure 25b, the spectrum is able to be observed.

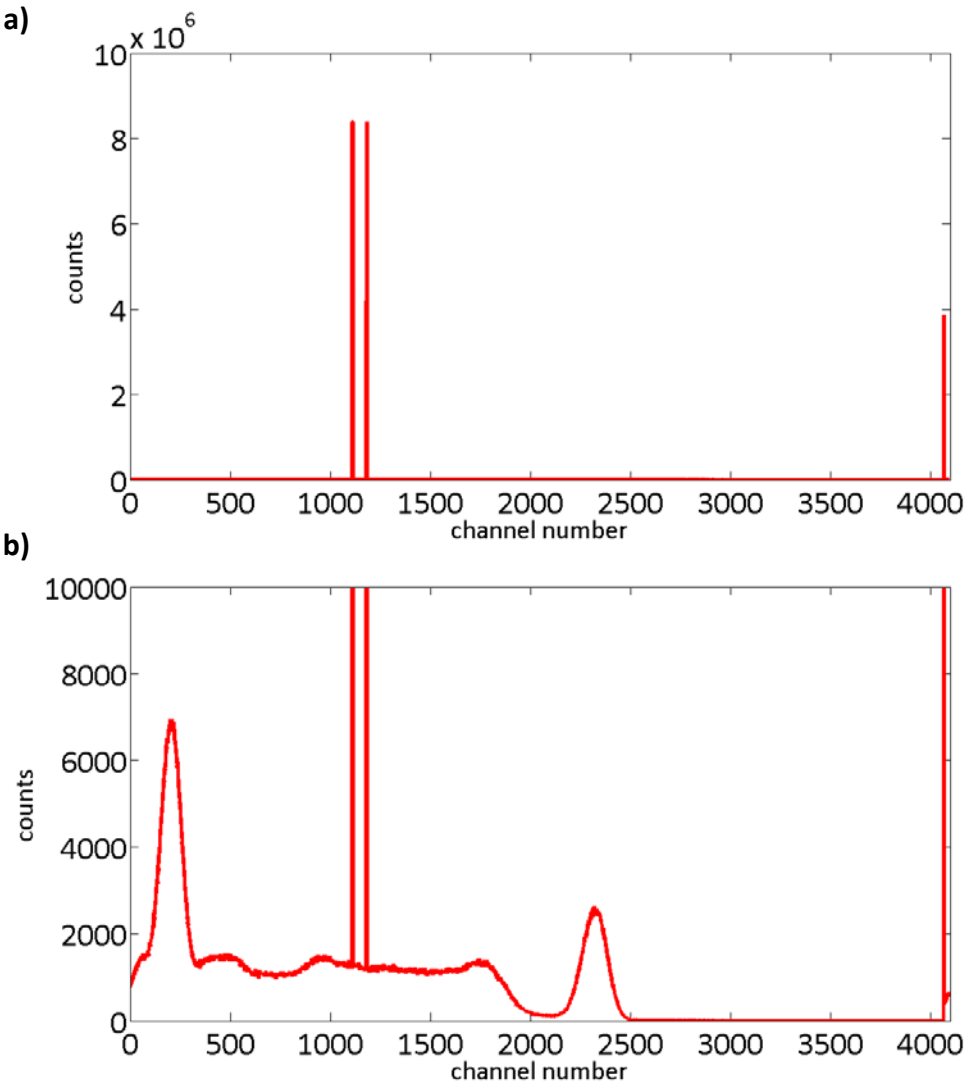

Figure 25. Example of spikes and channel-shifting phenomena.

In some measurements, the addresses of the memory read by the XEM6001 would appear to shift during the course of the measurement. This can be observed in figure 25b, where it appears that some of the channels near 4095 that would be continuous with the opposite end of addresses.

The reason for this phenomenon is the manner in which the trigger, trapezoidal shaper, and histogram interact. Because the trigger does not register pulses until they exceed the threshold set by the user, the temporal location of the peak sample may come after the flat portion of the trapezoidal shape, causing the result to be a negative number. Since the histogram does not account for negative numbers, the address instead “loops” around to the highest addresses. The “looped” addresses were eliminated by setting any “negative” value addresses to “0”. This address was then removed from the histogram plots. However, this temporary solution was not reached until after most measurements had been made, so all energy histograms in the energy resolution section have been plotted such that these “looped” addresses are not shown. This phenomenon does not impact the energy resolution of any of the full-energy peaks since none of them reach the section of addresses where these spikes appear.

In addition, large “spikes” could often be observed to appear and disappear during measurements and would, in rare cases, survive to the end of the measurement, also seen in figure 25. The reason for these phenomena is believed to originate in the transfer of data from the MiniSpec to the XEM6001, likely caused by the different and long length of each of the ribbon cables connecting the GPIO headers.

4.2. Pulse Waveform Characterization

The output pulses from the analog conditioning electronics were first characterized, both with square pulses from a pulse generator and with the detector and ^{137}Cs.

4.2.1. Square Waveform

First, a pulse generator was connected to the input of the preamplifier, and used to generate a 500 mV peak-to-peak, 100 Hz square wave to simulate noise [85] and the resulting waveform at various points through the analog conditioning chain was captured on an oscilloscope. Figure 26 shows the waveforms at a) the preamplifier output, b) the gain stage output, c) the RLC filter output, and d) in oscilloscope mode, respectively. Measurement points a)-c) are also labeled in figure 14 as TP1, TP2, and TP3, respectively.

To determine the noise contribution of the electronics to the system, waveforms were captured both with and without the detector attached, with no sources present. These waveforms were then centered around zero, and the root-mean-square (RMS) of each calculated. Since, in this case, the RMS is equal to the standard deviation of the signal, this can be converted directly to FWHM in keV. The noise added by the electronics from each setup is listed in table 5.

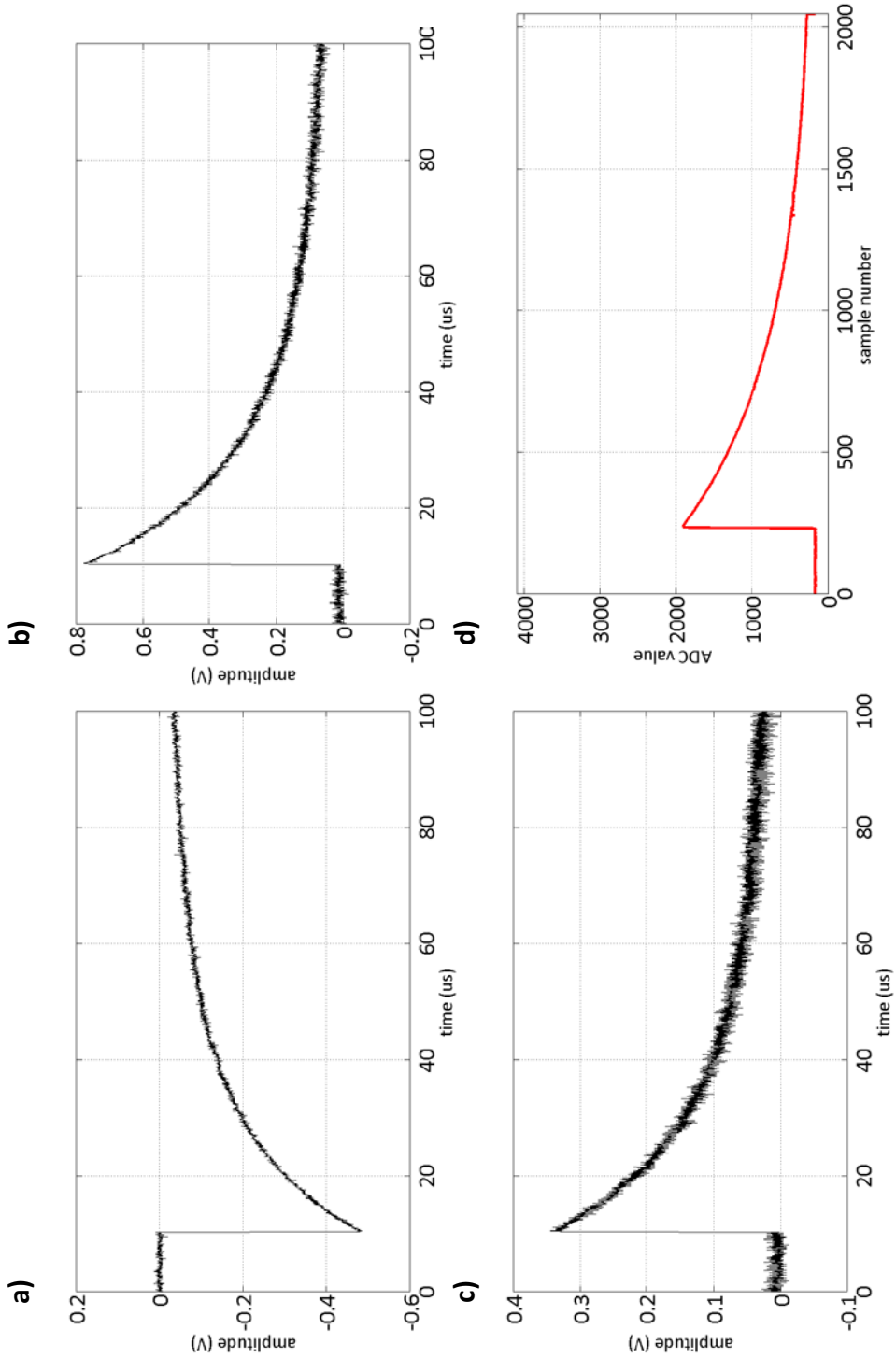

Figure 26. Pulse waveforms from a square input pulse a) at TP1, b) at TP2, c) at TP3, and d) after digitization.

Table 5. Electronic noise values.

setup	noise
without detector	0.5 keV (FWHM)
with detector	6.15 keV (FWHM)

The input capacitor for the signal generator was 330 pF. The amount of charge collected in a capacitor due to a given applied voltage is given by (7).

$$V = \frac{Q}{C}. \tag{7}$$

In the case of the signal generator input, *V* is the peak-to-peak voltage and *C* is the capacitance of the input capacitor, and *Q* is the injected charge. This relationship also holds for the voltage amplitude of the pulse that results from the preamplifier integration [15], where *Q* is instead the amount of charge collected in the preamplifier, *C* is the capacitance of the feedback capacitor, and *V* is the maximum amplitude of the resulting integrated pulse. The expected observed amplitude, in the case of the pulse generator, will be found by setting the charge generated on the capacitor by the signal generator equal to the input charge of the preamplifier. This calculation is made trivial since the input capacitance of the signal generator test point is equal to that of the preamplifier feedback capacitor.

Thus, the resulting peak amplitude seen at the preamplifier output as should be the same as the amplitude of the signal generator input. This can be observed in figure 26a: the amplitude of the pulse is -484 mV, which is well within the range

expected values (452 – 553 mV) given both capacitors possess a tolerance of ±5%.

In the gain stage of the analog conditioning electronics, the signal is amplified approximately 1.61 times, and the polarity inverted. Figure 26b shows the gain stage functioning as expected: the positive signal has an amplitude of 776 mV, or a gain of about 1.60 from the -484 mV input amplitude.

The relationship between the positive and negative outputs of the differential driver and the input is given by (8) [54]:

$$V_{OUT,dm} = \left(V_{+OUT} - V_{-OUT}\right), \tag{8}$$

where $V_{OUT,dm}$ is the combined output voltage, V_{+OUT} is the positive-polarity signal, and V_{-OUT} is the negative-polarity signal. In essence, the amplitude of each polarity should be half the amplitude of the total output signal. In this case, the amplitude of the total output signal should be equal to the amplitude of the input signal since the gain of the differential driver is unity. The amplitude of the pulse that results from the output of the differential driver and the RLC filter is 344 mV, which is slightly less than half of the input voltage. The source of this deficiency is unclear since the ±1% tolerances of the 510 Ω feedback resistors should only reduce the signal to about 380 mV at minimum. However, since this waveform was not captured from the same input waveform as that which produced the 776 mV gain stage output, it may be the result of statistical fluctuation.

The time constant for the square pulses was calculated using (9):

$$t_d = t_{37\%} - t_{\max}, \tag{9}$$

where τ is the time constant, $t_{37\%}$ is the time at which the pulse reaches e^{-1}, or approximately 36.78% of its amplitude on the falling edge, and t_{max} is the time at which the amplitude is observed. Since the digitized waveform in the FPGA did not possess units of time, the difference in sample numbers was multiplied by 25 ns, the period of the system clock, to convert the numbers of samples to units of time. The time constants for the pulses in figure 26 a)-d) were 21.76 μs, 22.52 μs, 23.16 μs, and 16 μs, respectively. The reason for the marked difference between the time constants of the digitized signal and those of the test points is due to the bandwidth of the oscilloscope.

The rise time of the square pulses was not able to be calculated using standard methods [50] due to its very short duration, so the time between the start of the pulse and the time of peak amplitude was taken as the rise time. The rise times for the pulses in figure 26a)-d) were 0.22 μs, 0.28 μs, 0.40 μs, and 0.125 μs, respectively. The reason for the marked difference between the rise time of the digitized signal and those of the test points is due to the bandwidth of the oscilloscope.

4.2.2. Detector Waveform

The same test points were used to capture pulses from the detector generated by a ^{137}Cs source. Figure 27 shows the waveforms at a) the preamplifier output,

b) the gain stage output, c) the RLC filter output, and d) in oscilloscope mode, respectively. As with the pulser measurements, measurement points a)-c) are also labeled in figure 14 as TP1, TP2, and TP3, respectively. Figure 28 shows a ^{137}Cs pulse captured in the FPGA oscilloscope mode with the different timing locations labeled.

The time constant was calculated using (9), shown previously, and rise time [50] was calculated using (10):

$$t_r = t_{90\%} - t_{10\%}; \tag{10}$$

where t_r is the rise time, $t_{90\%}$ is the time at which the waveform reaches 90% of its amplitude, and $t_{10\%}$ is the time at which the waveform reaches 10% of its amplitude.

As with the square waveforms, the times for the digitized signal were calculated using the differences in sample numbers and the period of the sampling clock. The rise times for the detector pulses in figure 27a)-d) were 7.0 μs, 7.32 μs, 7.12 μs, and 6.075 μs. The time constants for the detector pulses in figure 27a)-d) were 26.08 μs, 26.16 μs, 26.32 μs, and 22.4 μs. Again, the reason for the marked difference between the rise and time constants of the digitized signals and those of the test points is due to the bandwidth of the oscilloscope.

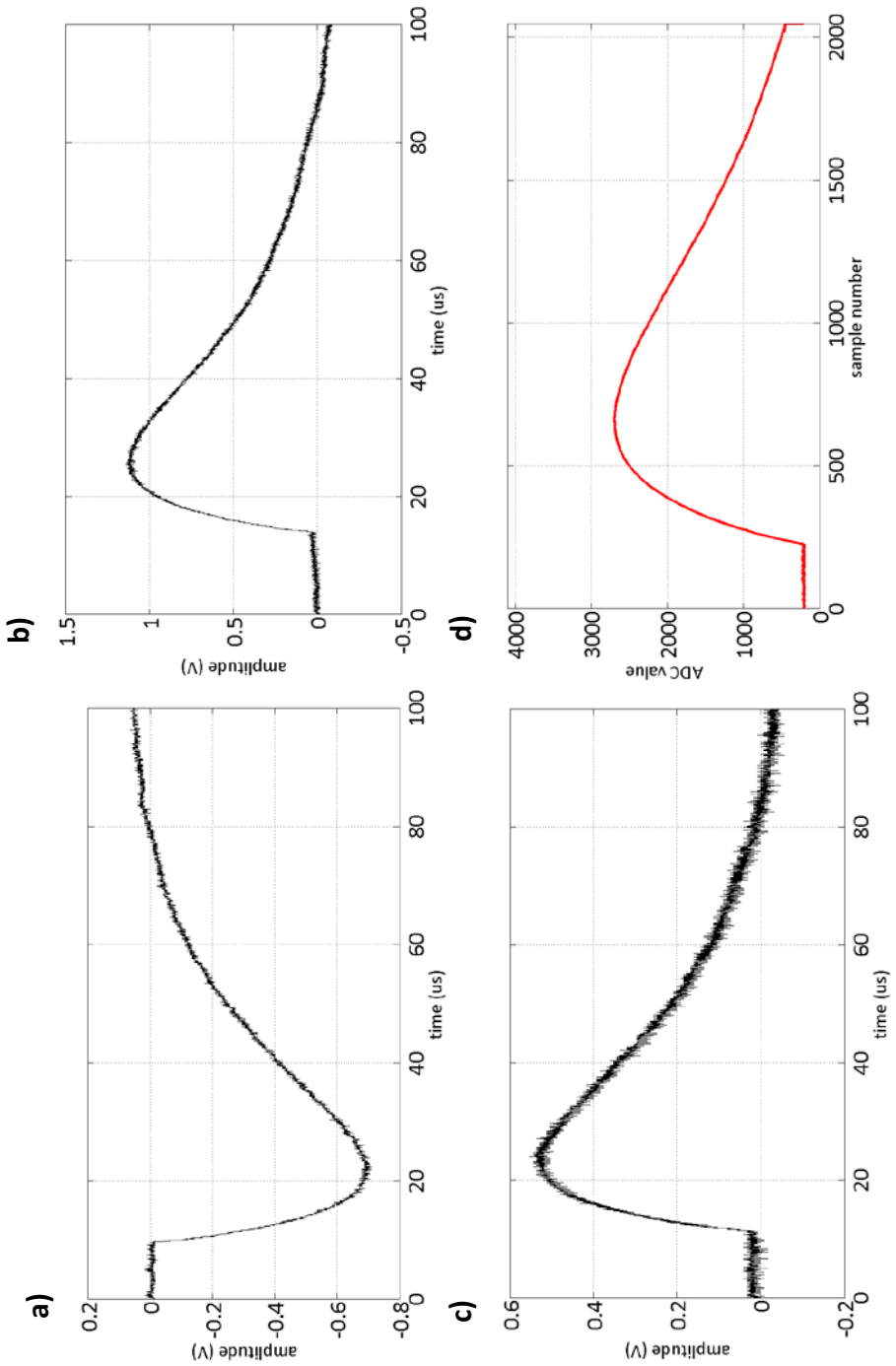

Figure 27. Pulse waveforms from the detector generated using ^{137}Cs a) at TP1, b) at TP2, c) at TP3, and d) after digitization.

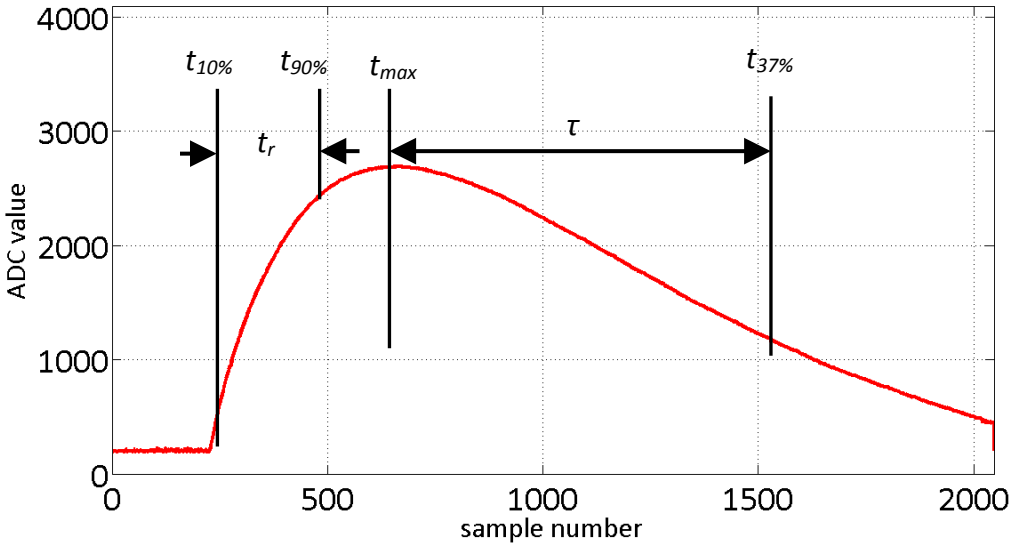

Figure 28. Digital pulse capture of pulse waveform from ^{137}Cs.

4.3. Peaking Time Characterization

The results of the peaking time measurements are shown in figure 29. Since peaking measurements were performed first, the flat time was chosen to be 0.5 µs in order to reduce pileup. The measure of peaking time performance was against the percent full-width, half-maximum (FWHM) resolution [15] of the 661.657 keV gamma ray peak from ^{137}Cs. The optimum peaking time is shown to be 20 µs. However, the trend of the measurements does not follow as closely the expected trend of resolution versus peaking time, which should be the same trend as noise energy versus peaking time [50].

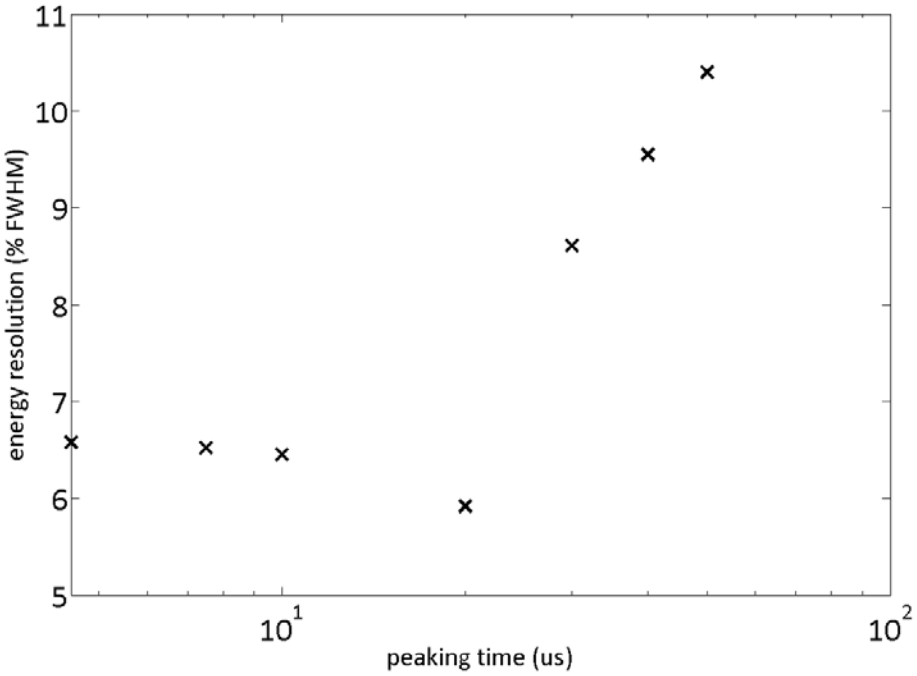

Figure 29. FWHM energy resolution of ^{137}Cs at 662 keV versus trapezoidal peaking time.

4.4. Flat Time Characterization

The results of the flat time measurements are shown in figure 30. The measure of flat time performance was again against the percent FWHM resolution of the 661.657 keV gamma ray peak from ^{137}Cs. The optimum peaking time of 20 µs was used for all measurements. The optimum flat time is shown to be 0.25 µs. This is expected as a longer overall trapezoidal shape will result in greater noise contribution, degrading the energy resolution [86]. Thus, the shortest flat time is expected to yield the best energy resolution performance.

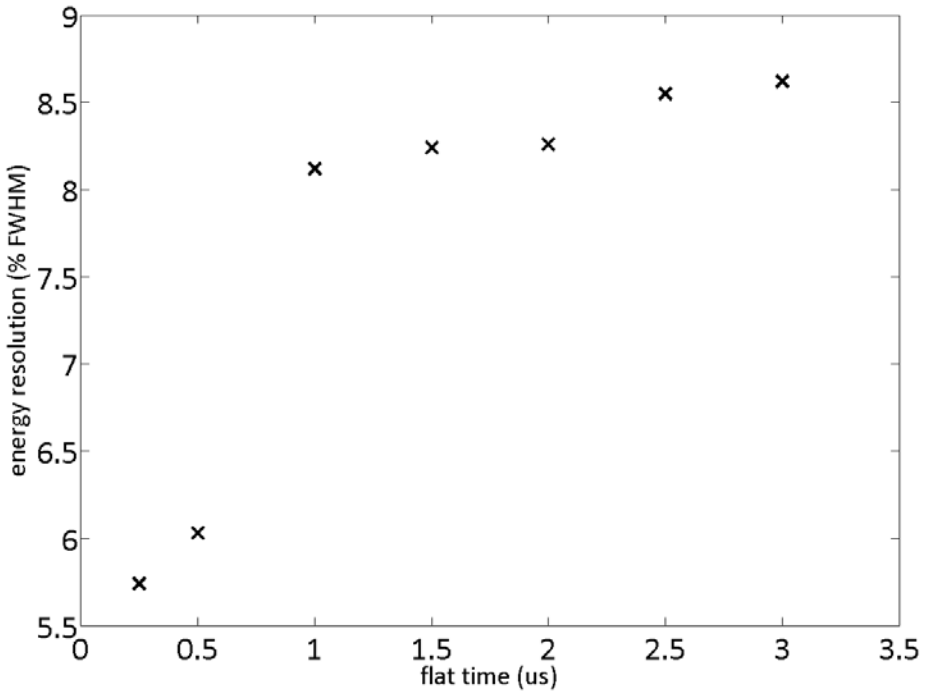

Figure 30. FWHM energy resolution of ^{137}Cs at 662 keV versus trapezoidal flat time.

4.5. Full-Energy Peak Characterization

All measurements in the full-energy peak set were conducted with the same trigger threshold, with pileup rejection on, with a peaking time of 20 µs, a flat time of 0.25 µs, and were run for one hour of live time.

4.5.1. Linearity and Dynamic Range

The full-energy peak set of measurements was used to determine the dynamic range and linearity. The full-energy peak centroid was determined by finding the

channel number in the peak, or region of interest (ROI), with the largest number of counts. The results are shown in figure 31.

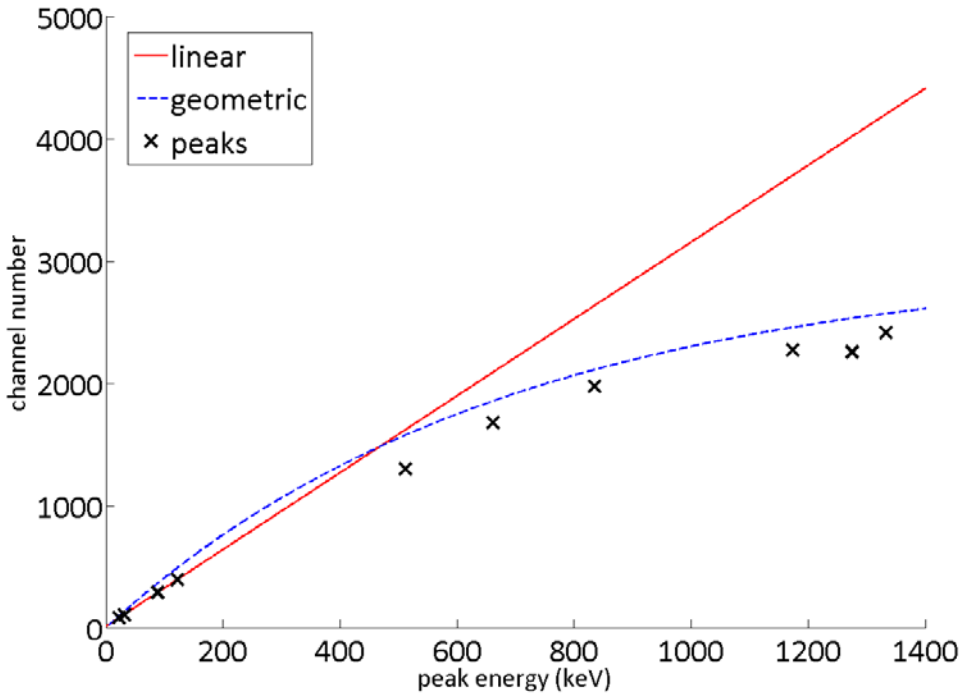

Figure 31. Channel number as a function of peak energy, with trend lines .

In this figure, a linear trend line is shown, which was calculated using MATLAB, and based on the four lowest-energy peaks. While these four are shown to follow this linear trend closely, the locations of higher-energy peak centroids diverge from this trend. However, this is expected for SSPM devices, as previously discussed. Thus, in (3), the maximum channel number can be substituted for M, and N_{fired} becomes the channel number incremented by absorption of a given number of photons. This equation was used to generate the "geometric" trend line seen in figure 31, with N_{ph} equal to the number of

photons per MeV [42], multiplied by the energy, and the *PDE* equal to the listed PDE of the SSPM [43] multiplied by the total fill-factor [46] to account for the dead space between microcells. *M* was found iteratively by simply using different values until a trend close to the peak centroid was found. For the geometric trend in figure 31, *M* is 3000 channels. The peak centroids conform to the geometric trend much more closely, indicating that the non-linearity can be primarily attributed to saturation of the SSPM microcells. Light reflection between optical boundary layers of the CsI(Tl), optical grease, and SSPM, and non-linearity of CsI(Tl) [87] could account for additional non-linearity of the system, bringing the geometric trend line closer to the plotted peak centroids.

Based on the equation from Stewart, the maximum energy able to be measured by the system is about 44.0 MeV, the point at which all microcells are triggered. However, each IC in the analog conditioning chain has limits to its input and output voltages. The output of the OPA656 can accommodate up to -3.3 V, which is just greater than the -3.03 V maximum that can be generated by a pulse from the SSPM. The OPA847 is able to accommodate up to 3.3 V at its input, and is able to output up to 3.3 V as well. Provided the gain is not more than 1.0891, the OPA847 will not be a limiting factor. The AD8138 can accommodate up to 3.2 V on this single-ended input, so a slight reduction in gain would be necessary. The AD8138 can accommodate up to 2.9 V peak-to-peak at the output, which is scaled from the input. However, the ADC input only ranges from 0 to 2 V peak to peak. Thus, the system can only send a maximum of 2.0 V through the analog processing chain to the differential driver to avoid the signal being out of range for the ADC. Based on the current system configuration, the 661.657 keV gamma ray from ^{137}Cs produces a -712 mV peak amplitude pulse (shown in figure 27a).

Based on a simpler linear extrapolation, the maximum energy that can be measured by the MiniSpec prototype is about 1.858 MeV.

The minimum measureable energy is determined by the trigger threshold set in the MATLAB interface. The energy-equivalent of the threshold setting was determined by convoluting a 662 keV pulse from ^{137}Cs with the triangular shaping filter in the trigger module in the FPGA. Based on a simple linear extrapolation, the minimum energy measureable by the MiniSpec should be about 59 keV. However, the 22.163 keV energy peak from ^{109}Cd was clearly visible, as discussed in the next section. Therefore, the minimum measureable energy is at most 22.163 keV.

4.5.2. Energy Resolution

The energy spectra collected from the isotopes listed in section 3.3 are shown in figures 32 through 37, with the percent FWHM energy resolution of each discernible peak labeled. All energy estimates that follow are calculated using the geometric trend from figure 31.

Both the 22 keV and 88 keV peaks can be observed in figure 32. Other figures show fairly large numbers of counts in their lower channels; this is because the threshold was set low enough in all measurements for the 22 peak of ^{109}Cd to be clearly observed.

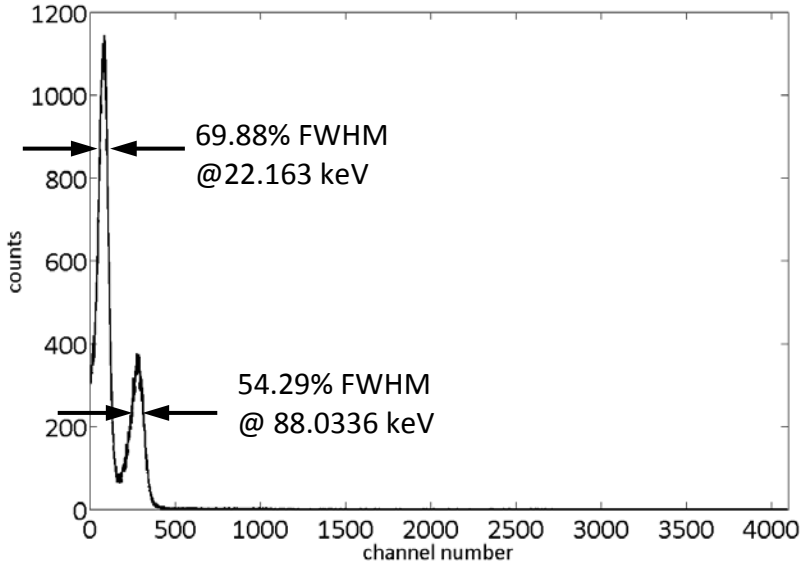

Figure 32. ^{109}Cd energy spectrum.

Figure 33 shows only one peak for ^{57}Co. The 136 keV peak centroid should appear at about channel 442, which is well inside the peak shown in figure 35. Given the lower intensity of the 136 keV peak, the peak in figure 35 was determined to be mostly due to the 122 keV peak and treated as such. Thus it is likely that there is some error in the resolution calculation of this peak. However, the extent of that error is unknown since the 136 keV peak cannot be observed and therefore cannot be measured.

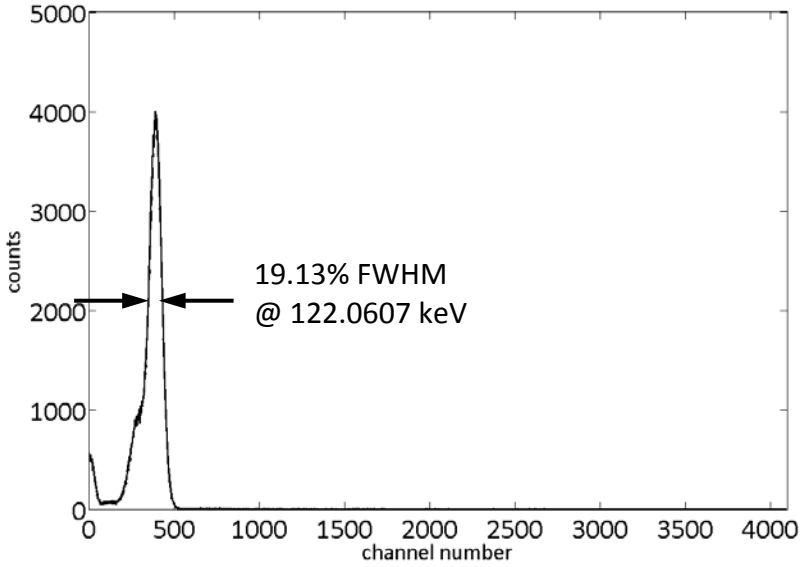

Figure 33. ^{57}Co energy spectrum.

Figure 34 shows both the 1173 and 1332 keV peaks of ^{60}Co. It also shows eight different identifiable spectrum features, correspondingly labeled one through eight. Features one and four are the double- and single-escape peaks, respectively, from the 1173 keV ^{60}Co gamma ray. Feature two is a backscatter peak at about 225 keV, in the middle of the expected range for backscatter energies [15]. Features three and five are the double- and single-escape peaks, respectively, from the 1332 keV ^{60}Co gamma ray. One reason that the height of the double-escape peak for 1173 is greater than that of 1332 might be that it is superimposed on the 78 keV escape peak from lead present in the setup. Finally, features six and seven are the Compton edges generated by the 1173 and 1332 keV ^{60}Co gamma rays, respectively.

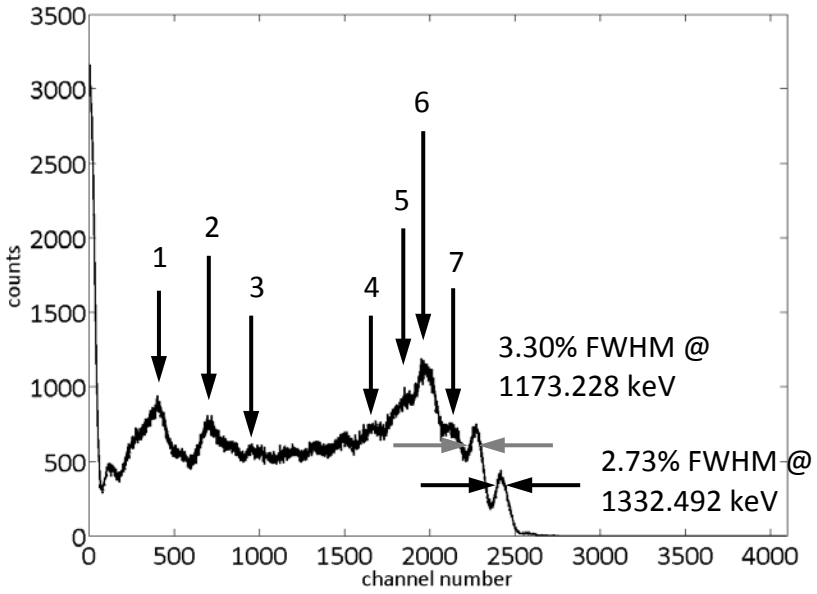

Figure 34. ^{60}Co energy spectrum.

As shown in figure 35, the best FWHM energy resolution at 662 keV was 5.66%, a vast improvement over previous measurements with the same SSPM and crystal [46]. This resolution is also comparable to other, similar devices [88], and even exceeds the manufacturer's own measurements (private conversation with SensL). The peak labeled "32.194 keV" is likely a result of both the 31.817 and 32.194 keV X-rays emitted during the ^{137}Cs decay process [83]. Since the 32 keV peak has a greater yield, the peak in figure 36 is labeled as such. Two features are also labeled in figure 37. Feature one is the backscatter peak caused primarily by the lead shielding in the setup, and feature two is the Compton edge generated by the 662 keV gamma ray from ^{137}Cs.

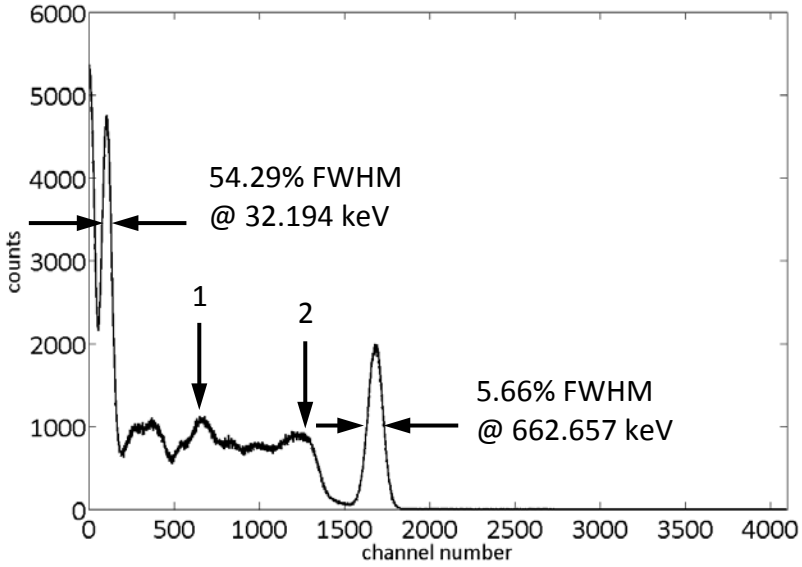

Figure 35. ^{137}Cs energy spectrum.

Figure 36 shows the ^{54}Mn spectrum with the 834.848 keV full-energy peak. Like the ^{137}Cs spectrum, its two labeled features are 1) the backscatter peak and 2) the Compton edge generated by the 834.848 keV from ^{54}Mn.

Figure 37 shows the ^{22}Na spectrum. The 1274 keV full-energy peak can be clearly observed. The annihilation peak at 511 keV is caused by annihilation interactions between positrons emitted during the ^{22}Na decay process [83] and electrons in the source itself. Since these annihilation interactions produce two 511 keV photons that are emitted in the opposite direction, only a 511 keV peak is observed and not a 1022 keV peak. Finally, four features are present in the ^{22}Na spectrum. Feature one is the backscatter peak caused by the lead present in the setup. Feature two is the double-escape peak from the 1274 keV gamma ray generated by ^{22}Na. No discernible single-escape peak was observed, though it is

predicted to be close to channel 1769. Features three and four are the Compton edges of the 511 and 1274 keV full-energy peaks, respectively.

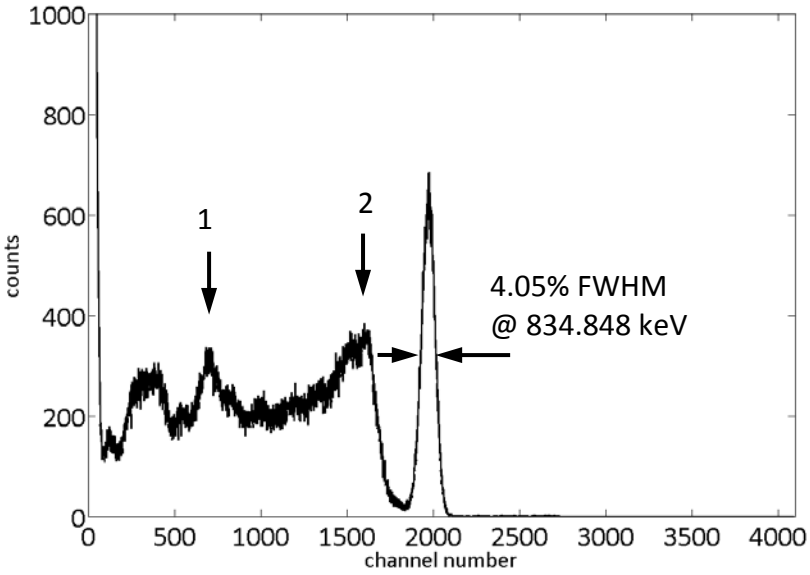

Figure 36. ^{54}Mn energy spectrum.

Figure 38 shows the percent FWHM energy resolution as a function of the full-energy peak centroid. Figure 38 also shows a theoretical fit, the equation for which is given by (11) [15]:

$$R = \frac{2.35}{\sqrt{N}}, \tag{11}$$

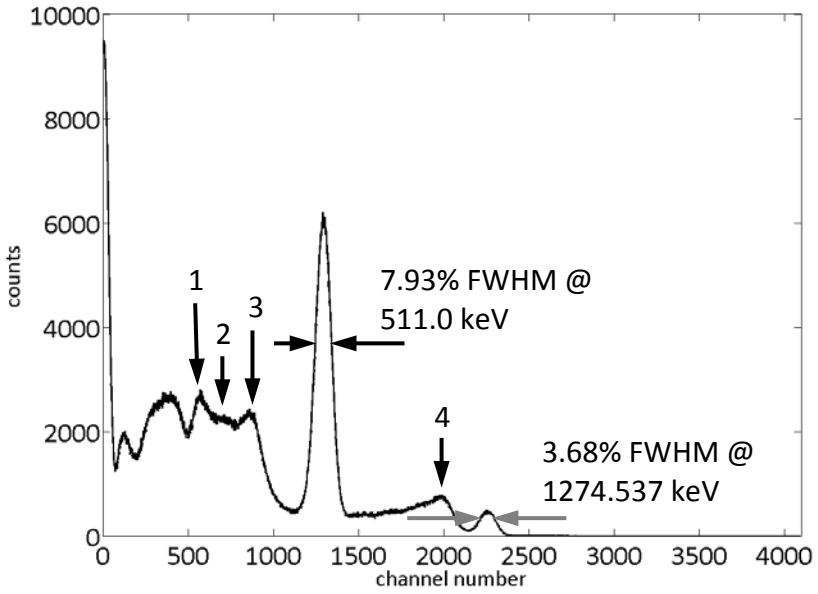

Figure 37. ^{22}Na energy spectrum.

where *N* is calculated in the same manner as the numerator in the exponent of (9) to more accurately represent the number of photons that trigger any of the SSPM microcells. This trend holds well for higher energies, but does not for lower energies. There are a number of factors that could contribute to this discrepancy. The first is the electronic noise added to the system. Since this added noise is a constant value, the difference between the theoretical and actual values will be more severe at lower energies. Another source of error could be scatter events that deposit energy between the source and CsI(Tl) crystal, thus reducing the number of photons generated in the CsI(Tl) crystal. Finally, average optical losses between the crystal, optical grease, and detector, could also result in wider FWHM, which would be accentuated for lower energies.

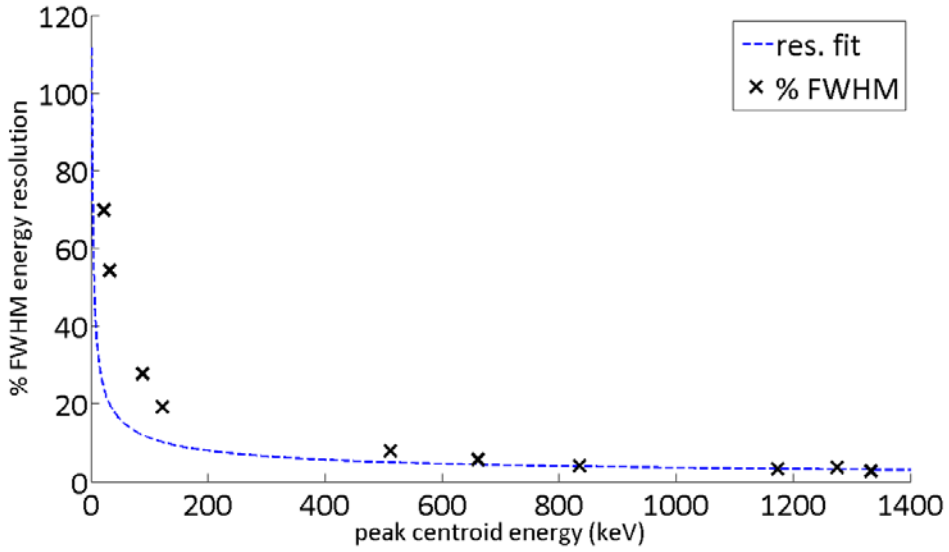

Figure 38. Percent FWHM energy resolution as a function of full-energy peak centroid with theoretical fit.

This resolution performance is better than other scintillators used with similar devices, such as LFS-3 [89], LSO:Ce, BGO [88], and LYSO [34], though $LaBr_3$ has been shown to outperform CsI(Tl) [88].

4.6. Full-Energy Peak Efficiency

The full-energy peak intrinsic efficiency was determined for full-energy peaks according to the procedures found in ANSI/IEEE Standard 325-1986 [90]. The four lowest-energy peaks were indiscernible from background and noise in the efficiency measurements, and are therefore not included here.

Figure 39 shows the full-energy peaks that were analyzed for intrinsic efficiency. Both the measured efficiency and the theoretical efficiency obtained using MCNP5 are plotted.

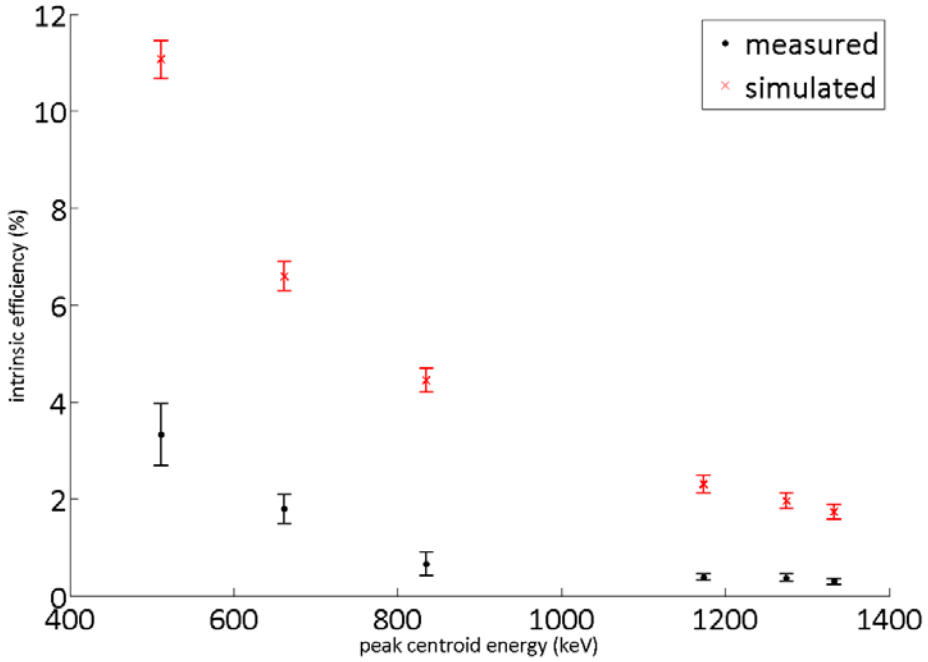

Figure 39. Simulated and measured intrinsic efficiency for full-energy peaks.

The measured intrinsic photopeak efficiencies are significantly less than those generated using MCNP5. However, there are several sources of count-loss from the full-energy peaks that are not taken into account in the MCNP calculations. Such sources might include attenuation by the light-shield and the reflective coating on the CsI(Tl) crystal. In addition, the MCNP simulation does not account for system dead time and pileup events. Finally, error bars on the measured efficiencies are not

4.7. Pileup

The pileup measurements were run for one hour each, once with pileup rejection enabled and disabled. The dead time is defined as the "minimum amount of time that must separate two events in order that they be recorded as two separate pulses" [15]. Using this definition, the total amount of live time and real time were recorded, and the dead time calculated using (12):

$$t_D = \frac{t_R - t_L}{t_R}, \tag{12}$$

where t_D is the dead time, t_R is the "real time", or the time as would be clocked by a stopwatch, and t_L is the "live time", or the amount of time over the course of the measurement that the system is able to accept new pulses. The percent dead time and percent FWHM energy resolution for 662 keV for each pileup setting are shown in table 6. The dead time per event in the MiniSpec is 150 ns. This was calculated by counting the number of states in the state machine after the peak is sampled, and the system is blind to any incoming pulses, and multiplying this number by the clock period.

The results shown in table 6 indicate that the pileup rejection setting is functional. The dead time is larger when pileup rejection is enabled since the time spent waiting for the signal to return to the baseline adds dead time to the system. The two spectra are shown in figure 40.

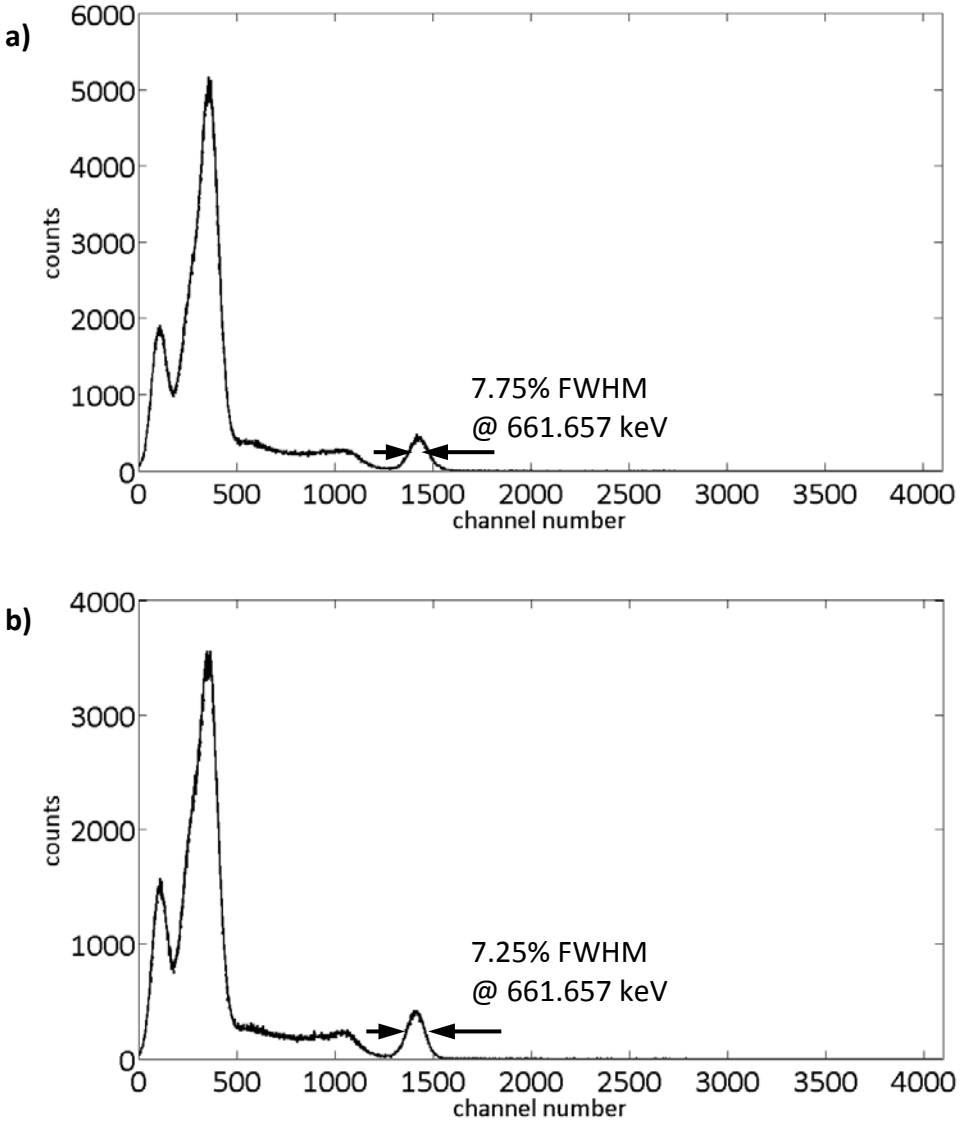

Figure 40. Spectra from ^{109}Cd, ^{57}Co, and ^{137}Cs with pileup rejection a) disabled and b) enabled.

Table 6. Percent dead time and percent FWHM at 662 keV corresponding to different pileup settings.

pileup setting	dead time	%FWHM @ 662 keV
disabled	0.01%	7.75%
enabled	0.04%	7.25%

5. CONCLUSIONS

5.1. Current Work

The functional MiniSpec prototype constructed as described herein as well as the characterization of the device fulfills most of the goals of this project. A small, low-power, digital gamma-ray spectrometer was successfully designed, constructed, and tested. The device is based on a SSPM coupled to a CsI(Tl) crystal for the detector and an FPGA-based digital pulse processor. The device requires only one 3.7 V input to power all on-board electronics and is compatible with a Flyport webserver for wireless access.

An external USB-interface board was connected to the MiniSpec for characterization, and MATLAB used as the control interface. The pulse shapes from both a square wave as well as pulses from ^{137}Cs using the SSPM were characterized and their agreement with expected theoretical values evaluated. The optimum peaking and flat times, 20 μs and 0.25 μs, respectively, were determined using a range of different settings for each and calculating the best percent FWHM energy resolution of ^{137}Cs. Ten different full-energy peaks from six different radioisotopes were measured using this device, and the non-linear trend in channel number versus full-energy peak centroid was identified and explained. The dynamic range of the MiniSpec is estimated to be between about 22 keV and 1.8 MeV. The energy resolution measurements yielded 5.66% FWHM energy resolution at 662 keV. Spectrum features in each of the histograms generated by the six sources were also identified. The intrinsic photopeak efficiency was characterized, and was determined to be 1.79% for 662 keV. The

noise introduced by the electronics was determined to be 6.15 keV (FWHM). Finally, the efficacy of the pileup rejection algorithm was verified and a dead time of 150 ns per event was calculated.

Finally, issues and deficiencies of the system were identified and explained throughout the characterization sections. Possible solutions to these issues are discussed in the next section.

5.2. Future Work

The MiniSpec prototype discussed in this thesis does not encompass the entirety of the functionality it was intended to possess. As mentioned in several sections, aspects of the original design were left unaddressed or incomplete due to time constraints.

5.2.1. Temperature Correction

One of the most important of unaddressed aspects is temperature correction. Since the SSPM is very sensitive to temperature, changes in temperature while the device is measuring a source will lead to decreased resolution since the centroids of any peaks will shift during the measurement, broadening the peak. In addition, higher temperatures, even constant, will degrade the performance of the detector since more thermal noise is introduced to the system via the SSPM as mentioned previously. This also broadens any energy peaks, which makes radionuclide identification more difficult. Data from the Maxim DS1822 temperature sensor was intended to be used in conjunction with the known

temperature dependence of the SSPM bias voltage as a method for temperature correction. The amplitude of pulses acquired would be adjusted based on the temperature at the given time. This would allow the MiniSpec to adjust values in real-time and maintain the ability for peak identification in real-time as well. Other methods, such as a self-adjusting analog circuit [91], involve additional cost and physical system complexity. Of greater interest for the MiniSpec are algorithms that can be implemented in the FPGA, such as one based on a light pulser. Different methods should be explored to determine the design that involves the lowest cost and least physical complexity. These methods should be tested using a controlled environment chamber to maintain precise control over the temperature.

5.2.2. Pulse Processing

Another aspect of the design that could be improved upon is the pulse processing firmware in the FPGA. As previously mentioned, the trapezoidal filter is based on a step-function input, while the real input has measurable rise time and time constant. Improving this shaping firmware to account for a real pulse should lead to improved resolution. In addition, the trigger firmware should be changed to rely on a constant fraction discriminator [92] [93] instead of a triangular filter. Since the rise time of the pulses is significant, the time that the system is triggered varies with relation to the time when the pulse reaches its maximum amplitude. This affects when the histogram algorithm samples the pulse, which can lead to erroneous samples, as discussed previously. When using a constant fraction discriminator, the trigger occurs at the peak of the pulse every time.

5.2.3. Miscellaneous

Additional ways to improve and characterize the MiniSpec include:

- completion of the Flyport wireless interface,
- replacing the FPGA with a smaller Spartan 6 model, with a larger number of GPIOs,
- fully optimizing components for a balance of high-performance, low-power,
- stabilization and optimization of SSPM bias voltage,
- purpose-fit components for connection to a mobile phone battery,
- performance assessment when connected to battery,
- implementation of an application for mobile devices,
- implementation of an isotope-identification algorithm, and
- implementation of a dosimetry calculation algorithm.

Finally, future work should include a second prototype, using a re-designed, smaller PCB with improved circuit-design techniques, such as on-board test points. This board should be able to be mounted in a custom enclosure that is able to accommodate a mobile phone battery and the Flyport in order to demonstrate a possible commercial device.

Bibliography

[1] IAEA, WCO, EUROPOL, and INTERPOL, "Detection of radioactive materials at borders," International Atomic Energy Agency, Vienna, Austria, 2002.

[2] US Department of Homeland Security, *Basic Handheld Radioisotope Identification Device: Request for Proposal,* 2013.

[3] US Environmental Protection Agency, "Radiation Protection," 14 February 2013. [Online]. Available: http://www.epa.gov/radiation/rert/rert.html. [Accessed 27 June 2013].

[4] US Department of Health and Human Services, "Radiation Emergency Medical Management," [Online]. Available: http://www.remm.nlm.gov/index.html. [Accessed 27 June 2013].

[5] CTIF, IAEA, PAHO, WHO, "Manual for First Responders to a Radiological Emergency," IAEA, Vienna, Austria, 2006.

[6] D. Oldenburg, "Detection Devices May Offer an Early Read on the Danger," The Washington Post, [Online]. Available: http://www.washingtonpost.com/wp-srv/health/specials/preparedness/detection.html. [Accessed 27 June 2013].

[7] RAE Systems, "Radiation Detection: Selecting the Right Equipment for the Job," RAE Systems, San Jose, USA, 2011.

[8] US National Nuclear Security Administration, "Nuclear Emergency Support Team (NEST)," 17 April 2013. [Online]. Available: http://www.nv.doe.gov/library/FactSheets/NEST.pdf. [Accessed 27 June 2013].

[9] A. J. Caffery, et al., "Chemical Warfare Agent and High Explosive Identification by Spectroscopy of Neutron-Induced Gamma Rays," *IEEE Trans. Nucl. Sci.,* vol. 39, no. 5, pp. 1422-1426, 1992.

[10] T. Burr and M. Hamada, "Radio-Isotope Identification Algorithms for NaI γ Spectra," *Algorithms,* vol. 2, no. 1, pp. 339-360, 2009.

[11] M. T. Batdorf, et al., "Isotope Identification in the GammaTracker," in *Nucl. Sci. Symposium*, 2009.

[12] R. M. Keyser, T. R. Twomey and D. L. Upp, "A Comparison of an HPGe-based and NaI-based Radionuclide," in *ESARDA Annual Meeting*, 2005.

[13] F. Flakes, "Detecting and measuring ionizing radiation - a short history,"

IAEA Bulletin, vol. 23, no. 4, pp. 31-36, 1982.

[14] J. K. Shultis and R. E. Faw, Radiation Shielding, La Grange Park, USA: American Nuclear Society, 2000.

[15] G. F. Knoll, Radiation Detection and Measurement, Hoboken, USA: John Wiley & Sons, Inc., 2000.

[16] A. Compton, "A Quantum Theory of the Scattering of X-Rays by Light Elements," *The Physical Review,* vol. 21, no. 5, pp. 483-502, 1923.

[17] R. Hofstadter, "Alkali Halide Scintillation Counters," *Physical Review,* vol. 74, no. 1, pp. 100-101, 1948.

[18] R. B. Murray and F. J. Keller, "Recombination Luminescence from Vk Centers in Potassium Iodide," *Physical Review,* vol. 137, no. 3A, pp. 942-948, 1965.

[19] J. T. Randall and M. H. F. Wilkins, "Phosphorescence and electron traps I. The study of trap distributions," *Proc. Royal Society of London A, Math. Phys. Sci.,* vol. 184, no. 999, pp. 365-389, 1945.

[20] R. McIntrye, "Theory of Microplasma Instability in Silicon," *J. Appl. Phys.,* vol. 32, no. 6, pp. 983-995, 1961.

[21] R. Haitz, "Model for the Electrical Behavior of a Microplasma," *J. Appl. Phys.,* vol. 35, no. 5, pp. 1370-1376, 1964.

[22] D. Renker, "Geiger-mode avalanche photodiodes, history, properties and problems," *Nucl. Instr. Meth. A,* vol. 567, no. 1, pp. 48-56, 2006.

[23] S. Vasile, "High Gain Avalanche Photodiode Arrays for DIRC Applications," *IEEE Trans. Nucl. Sci.,* vol. 46, no. 4, pp. 848-852, 1999.

[24] V. Saveliev and V. Golovin, "Silicon avalanche photodiodes on the base of metal-resistor-semiconductor (MRS) structures," *Nucl. Instr. Meth. A,* vol. 442, no. 1, pp. 223-229, 2000.

[25] SensL, "Silicon Photomutlipliers," 2013. [Online]. Available: http://sensl.com/products/silicon-photomultipliers/. [Accessed 28 June 2013].

[26] Hamamatsu, "MPPC (multi-pixel photon counters)," [Online]. Available: http://www.hamamatsu.com/us/en/product/category/3100/4004/index.html. [Accessed 28 June 2013].

[27] J. Ninkovic, "Recent developments in silicon photomultipliers," *Nucl. Instr. Meth. A,* vol. 580, no. 2, pp. 1020-1022, 2007.

[28] B. Dolgoshein, et al., "Status report on silicon photomultiplier," *Nucl. Instr.*

Meth. A, vol. 563, no. 2, pp. 368-376, 2006.

[29] D. Renker and E. Lorenz, "Advances in solid state photon detectors," *J. Instrumentation,* vol. 4, no. 4, 2009.

[30] M. D. Hammig, et al., "Development of Al Ga As Photodiodes for Use in Wide Band-Gap Solid-State Photomultipliers," *IEEE Trans. Nucl. Sci.,* vol. 60, no. 2, pp. 1175-1181, 2013.

[31] M. McClish, et al., "Characterization and scintillation studies of a solid-state photomultiplier," *Nucl. Instr. Meth. A,* vol. 572, no. 3, pp. 1065-1070, 2007.

[32] SensL, "An Introduction to the Silicon Photomultiplier," 21 October 2011. [Online]. Available: http://www.sensl.com/downloads/ds/TN%20-%20Intro%20to%20SPM%20Tech.pdf. [Accessed 28 June 2013].

[33] E. Rutherford and H. Geiger, "An Electrical Method of Counting the Number of α-Particles from Radio-Active Substances," *Proc. Royal Society of London A,* vol. 81, no. 546, pp. 141-161, 1908.

[34] A. G. Stewart, et al., "Performance of 1-mm^2 Silicon Photomultiplier," *IEEE Jrnl. Quant. Elect.,* vol. 44, no. 2, pp. 157-164, 2008.

[35] M. Ramilli, "Characterization of SiPM: temperature dependencies," in *IEEE Nucl. Sci. Symp. Conf. Record*, 2008.

[36] C. Tur, V. Solovyev and J. Flamanc, "Temperature characterization of scintillation detectors using solid-state photomultipliers for radiation monitoring applications," *Nucl. Instr. Meth. A,* vol. 620, no. 2, pp. 351-358, 2010.

[37] B. G. Streetman and S. K. Banerjee, Solid State Electronic Devices, Upper Saddle River: Prentice Hall, 2006.

[38] J. B. Simoes and C. M. Correia, "Pulse processing architectures," *Nucl. Instr. Meth. A,* vol. 422, no. 1, pp. 405-410, 1999.

[39] R. Grzywacz, "Applications of digital pulse processing in nuclear spectroscopy," *Nucl. Instr. Meth. B,* vol. 204, pp. 649-659, 2003.

[40] A. T. Farsoni and D. M. Hamby, "A system for simultaneous beta and gamma spectroscopy," *Nucl. Instr. Meth. A,* vol. 578, no. 3, pp. 528-536, 2007.

[41] J. M. Cardoso, et al., "A High Performance Reconfigurable Hardware," *IEEE Trans. Nucl. Sci,* vol. 51, no. 3, pp. 921-925, 2004.

[42] Hilger Crystals, "Properties of CsI(Tl)," 2013. [Online]. Available:

http://www.hilger-crystals.co.uk/properties.asp?material=7. [Accessed 6 July 2013].

[43] SensL, "MicroSL Silicon Photomultiplier Detectors Datasheet," January 2012. [Online]. Available: www.sensl.com. [Accessed November 2011].

[44] Saint-Gobain Crystals, "CsI(Tl), CsI(Na), Cesium Iodide Scintillation Material," 2012. [Online]. Available: http://www.detectors.saint-gobain.com/uploadedFiles/SGdetectors/Documents/Product_Data_Sheets/CsI(Na)-CsI(Tl)-Data-Sheet.pdf. [Accessed 13 August 2013].

[45] P. Schotanus, R. Kamermans and P. Dorenbos, "Scintillation characteristics of pure and T1-doped CsI crystals," *IEEE Trans. Nucl. Sci.,* vol. 37, no. 2, pp. 177-182, 1990.

[46] E. M. Becker, A. T. Farsoni, A. M. Alhawsawi and B. Alemayehu, "Small Prototype Gamma Spectrometer Using CsI(Tl) Scintillator Coupled to a Solid-State Photomultiplier," *IEEE Trans. Nucl. Sci.,* vol. 60, no. 2, pp. 968-972, 2013.

[47] Texas Instruments, "OPA656 Datasheet," 2013. [Online]. Available: http://www.ti.com/lit/ds/symlink/opa656.pdf. [Accessed 30 July 2013].

[48] Saint-Gobain Ceramis and Plastics, Ltd., "CsI(Tl), CsI(Na): Cesium Iodide Scintillation Material," 2008. [Online]. Available: http://www.detectors.saint-gobain.com/CsI(Tl).aspx. [Accessed 19 January 2012].

[49] S. Mukhopadhyay, P. Guss and R. Maurer, "Current Trends in Gamma Radiation Detection for Radiological Emergency Response," in *Proc. of SPIE, vol. 8144*, 2011.

[50] The Institute of Electrical and Electronics Engineers, *IEEE Standard Test Procedures forAmplifiers and Preamplifiers for Semiconductor Radiation Detectors for Ionizing Radiation, IEEE Std 301-1976,* IEEE, 1976.

[51] P. Horowitz and W. Hill, The Art of Electronics, 2nd ed., New York: Cambridge University Press, 2008.

[52] Texas Instruments, "OPA847 Datasheet," 2013. [Online]. Available: http://www.ti.com/lit/ds/symlink/opa847.pdf. [Accessed 30 July 2013].

[53] Nallatech Limited, "XtremeDSP Development Kit-IV User Guide," 2005. [Online]. Available: http://www.xilinx.com/support/documentation/boards_and_kits/ug_xtremedsp_devkitIV.pdf. [Accessed 5 July 2013].

[54] Analog Devices, "AD8138: LOW DISTORTION DIFFERENTIAL ADC DRIVER,"

2013. [Online]. Available: AD8138: LOW DISTORTION DIFFERENTIAL ADC DRIVER. [Accessed 30 July 2013].

[55] Analog Devices, "AD9629: 12-BIT, 20/40/65/80 MSPS, 1.8 V ANALOG-TO-DIGITAL CONVERTER," 2013. [Online]. Available: http://www.analog.com/static/imported-files/data_sheets/AD9629.pdf. [Accessed 30 July 2013].

[56] Xilinx, Inc., "Spartan-6 FPGA Family," 2013. [Online]. Available: http://www.xilinx.com/products/silicon-devices/fpga/spartan-6/. [Accessed 30 July 2013].

[57] Xilinx, Inc., "Platform Flash In-System Programmable Configuration PROMs," 19 May 2010. [Online]. Available: http://www.xilinx.com/support/documentation/data_sheets/ds123.pdf. [Accessed 30 July 2013].

[58] Abracon Corporation, "Plastic Package Industrial Grade Uultra Miniature Pure Silicon Clock Oscillator," 23 April 2013. [Online]. Available: http://www.abracon.com/Oscillators/ASDMB.pdf. [Accessed 30 July 2013].

[59] V. T. Jordanov and G. F. Knoll, "Digital synthesis of pulse shapes in real time for high resolution radiation spectroscopy," *Nucl. Instr. Meth. A,* vol. 345, no. 2, pp. 337-345, 1994.

[60] W. Kaye, et al., "Calibration and Operation of the Polaris," in *Nucl. Sci. Symposium Conference Record*, 2010.

[61] V. T. Jordanov, D. L. Hall and M. Kastner, "Digital Peak Detector with Noise Threshold," in *Nucl. Sci. Symposium Conference Record*, 2002.

[62] Maxim Integrated, "Econo 1-Wire Digital Thermometer," 2013. [Online]. Available: http://datasheets.maximintegrated.com/en/ds/DS1822.pdf. [Accessed 30 July 2013].

[63] Maxim Integrated, "500kHz, 36V Output, SOT23, PWM Step-Up DC-DC Converters," 2013. [Online]. Available: http://datasheets.maximintegrated.com/en/ds/MAX5025-MAX5028.pdf. [Accessed 30 July 2013].

[64] Maxim Integrated, "MAX17067 Low-Noise Step-Up DC-DC Converter," 2013. [Online]. Available: http://datasheets.maximintegrated.com/en/ds/MAX17067.pdf. [Accessed 30 July 2013].

[65] Maxim Integrated, "MAX889 High-Frequency, Regulated, 200mA, Inverting

Charge Pump," 2013. [Online]. Available: http://datasheets.maximintegrated.com/en/ds/MAX889.pdf. [Accessed 30 July 2013].

[66] Linear Technologies, "LT03032 Series: Dual 150mA Positive/Negative Low Noise Low Dropout Linear Regulator," 2013. [Online]. Available: http://cds.linear.com/docs/en/datasheet/3032fd.pdf. [Accessed 30 July 2013].

[67] Texas Instruments, "Triple-Supply Power Management IC for Powering FPGAs and DSPs," 2010. [Online]. Available: http://www.ti.com/lit/ds/symlink/tps75003.pdf. [Accessed 30 July 2013].

[68] Texas Instruments, "Cap-Free, NMOS, 250mA Low Dropout Regulator with Reverse Current Protection," 2010. [Online]. Available: http://www.ti.com/lit/ds/symlink/tps73201.pdf. [Accessed 30 July 2013].

[69] Opal Kelly, "XEM6001," 2013. [Online]. Available: http://www.opalkelly.com/products/xem6001/. [Accessed 30 July 2013].

[70] The MathWorks, Inc., "MATLAB, v.2012b," 2013. [Online]. Available: http://www.mathworks.com/products/matlab/?s_tid=hp_fp_ml. [Accessed 04 August 2013].

[71] Opal Kelly, "FrontPanel User's Manual," 2012. [Online]. Available: http://assets00.opalkelly.com/library/FrontPanel-UM.pdf. [Accessed 07 July 2013].

[72] openPicus, "Flyport Wifi," 2 July 2013. [Online]. Available: http://wiki.openpicus.com/index.php/Flyport_WiFi. [Accessed 4 July 2013].

[73] Sunstone Circuits, "PCB123 - Free PCB Design Software," 2010. [Online]. Available: http://www.sunstone.com/PCB123.aspx. [Accessed 30 July 2013].

[74] "Sunstone Circuits," 2010. [Online]. Available: http://www.sunstone.com/. [Accessed 30 July 2013].

[75] "Screaming Circuits," 2011. [Online]. Available: http://www.screamingcircuits.com/. [Accessed 30 July 2013].

[76] N. Ledoux, "Breaking Ground Loops with Functional Isolation to Reduce Data Transmission Errors, MS-2256," December 2011. [Online]. Available: http://www.analog.com/static/imported-files/tech_articles/MS-2256.pdf. [Accessed 06 July 2013].

[77] R. Aiken, "Star Grounding," 5 May 11. [Online]. Available:

http://www.aikenamps.com/StarGround.html. [Accessed 06 July 2013].

[78] XRF Corporation, "ICS-4000 Handheld Radionuclide Identifier," 2008. [Online]. Available: http://www.radiation-measurement-systems.com/XRF_CORPORATION_Products.html. [Accessed 31 July 2013].

[79] D-tect Systems, "rad-ID Handheld Radiation Identifier," 2013. [Online]. Available: http://www.dtectsystems.com/rad-ID_page.html. [Accessed 13 July 2013].

[80] U. Cross, "A Survey Study of Commercially Available Handheld Radionuclide Identifiers," RHP 505, 2013.

[81] Spectrum Techniques, "Disc and Laminated Sources," 2013. [Online]. Available: http://spectrumtechniques.com/disc&laminated_sources.htm. [Accessed 7 July 2013].

[82] X-5 Monte Carlo Team, "MCNP - A General Monte Carlo N-Particle Transport Code, Version 5, Volume II: User's Guide," Los Alamos National Laboratory, Oak Ridge National Laboratory, Radiation Safety Information Computational Center, 2003.

[83] Brookhaven National Laboratory, "Interactive Chart of Nuclides," [Online]. Available: http://www.nndc.bnl.gov/chart/chartNuc.jsp. [Accessed 7 July 2013].

[84] R. G. Williams III, C. J. Gesh and R. T. Pagh, "Compendium of Material Composition Data for Radiation Transport Modeling," National Technical Information Service, US Department of Commerce, Springfield, VA, 2003.

[85] CREMAT, "CR-110 charge sensitive preamplifier fast application guide," [Online]. Available: http://www.fastcomtec.com/fwww/datashee/amp/cr-110.pdf. [Accessed 02 August 2013].

[86] V. Radeka, "Trapezoidal Filtering of Signals from Large Germanium Detectors at High Rates," *Nucl. Instr. Meth. ,* vol. 99, no. 3, pp. 525-539, 1972.

[87] A. Syntfeld-Kazuch, et al., "Non-Proportionality and Energy Resolution of CsI(Tl)," *IEEE Trans. Nucl. Sci.,* vol. 54, no. 5, pp. 1836-1841, 2007.

[88] M. Grodzicka, "2x2 MPPC Arrays in Gamma spectrometry with CsI(Tl), LSO:Ce(Ca), LaBr3, BGO," in *IEEE Nucl. Sci. Symp. Conf. Record*, 2011.

[89] M. Grodzicka, et al., "Energy resolution of scintillation detectors with SiPM light readout," in *Nucl. Sci. Symp. Conf. Record*, 2010.

[90] The Insitute of Electrical and Electronics Engineers, "IEEE Standard Test Procedures for Germanium Gamma Ray Detectors, ANSI/IEEE Std 325-

1986," IEEE, New York, 1986.

[91] F. Licciulli, I. Indiveri and C. Marzocca, "A Novel Technique for the Stabilization of SiPM Gain Against Temperature Variations," *IEEE Trans. Nucl. Sci.,* vol. 60, no. 2, pp. 606-611, 2013.

[92] D. A. Gedcke and W. J. McDonald, "Design of the constant fraction of pulse height trigger for optimum time resolution," *Nucl. Instr. Meth.,* vol. 58, no. 2, pp. 253-260, 1968.

[93] T. J. Paulus, "Timing electronics and fast timing methods with scintillation detectors," *IEEE Trans. Nucl. Sci.,* vol. 32, no. 3, pp. 1242-1249, 1985.